A coupled geochemical-geodynamical approach for predicting mantle melting in space and time

P. W. Ball[1,2], T. Duvernay[2], and D. R. Davies[2]

[1]Department of Geosciences, Colorado State University, Fort Collins, CO 80523, USA.
[2]Research School of Earth Sciences, Australian National University, Canberra, ACT 2601, Australia.

Key Points:

- We present the BDD21 peridotite-melting parameterization that can be coupled with geodynamical simulations to calculate melt composition
- BDD21 is applied to simulations of mid-oceanic ridges to replicate observed patterns of crustal thickness and melt chemistry
- Geodynamical simulations that incorporate BDD21 can be used to study melting adjacent to lithospheric steps and in other geologic settings

Corresponding author: P. W. Ball, patrick.ball@colostate.edu

Abstract

Geodynamical simulations underpin our understanding of upper-mantle processes, but their predictions require validation against observational data. Widely used geophysical datasets provide limited constraints on dynamical processes into the geological past, whereas under-exploited geochemical observations from volcanic lavas at Earth's surface constitute a valuable record of mantle processes back in time. Here, we describe a new peridotite-melting parameterization, BDD21, that can predict the incompatible-element concentrations of melts within geodynamical simulations, thereby providing a means to validate these simulations against geochemical datasets. Here, BDD21's functionality is illustrated using the Fluidity computational modelling framework, although it is designed so that it can be integrated with other geodynamical software. To validate our melting parameterization and coupled geochemical-geodynamical approach, we develop 2-D single-phase flow simulations of melting associated with passive upwelling beneath mid-oceanic ridges and edge-driven convection adjacent to lithospheric steps. We find that melt volumes and compositions calculated for mid-oceanic ridges at a range of mantle temperatures and plate-spreading rates closely match those observed at present-day ridges. Our lithospheric-step simulations predict spatial and temporal melting trends that are consistent with those recorded at intra-plate volcanic provinces in similar geologic settings. Taken together, these results suggest that our coupled geochemical-geodynamical approach can accurately predict a suite of present-day geochemical observations. Since our results are sensitive to small changes in upper-mantle thermal and compositional structure, this novel approach provides a means to improve our understanding of the mantle's thermo-chemical structure and flow regime into the geological past.

Plain Language Summary

Earth's mantle is a $\sim$ 3000 km thick layer of hot rock that lies between Earth's crust and core. Its slow, creeping, convective motion over billions of years has been integral to Earth's thermal, chemical, tectonic and geological evolution. However, an inability to reproduce observational constraints derived from the composition of volcanic lavas at Earth's surface limits our capacity to validate models of mantle convection back in time. Here, we present a new framework that can predict the volume and composition of melts generated within the mantle. These predictions compare favourably with those recorded by igneous rocks at Earth's surface in two geologic settings: mid-oceanic ridges, where plates move apart to drive decompression melting, and lithospheric steps, where instabilities associated with changes in the thickness of Earth's rigid outermost shell generate volcanism far from plate boundaries. The approach and tools presented here will allow scientists to better understand the mantle's past structure, dynamics, evolution and impact on Earth's surface.

1 Introduction

Geodynamical models are important tools for investigating the spatio-temporal evolution of the upper mantle across a wide variety of geologic settings (e.g., Houseman et al., 1981; Turcotte & Emerman, 1983; Bercovici et al., 1989; Tackley et al., 1993; Steinberger, 2000; Schellart et al., 2007). To assess how well geodynamical model predictions replicate uppermost mantle conditions, it is necessary to validate simulations against a diverse range of observations. To date, such comparisons have focused primarily on geophysical constraints, such as gravimetric, seismic tomographic, seismic anisotropic and dynamic topographic datasets (e.g., Becker et al., 2006; Forte et al., 2010; Garel et al., 2014; Davies et al., 2019; Cooper et al., 2021; Ghelichkhan et al., 2021). These geophysical observations are confined to the present day and, hence, offer limited information on the thermo-chemical structure of the uppermost mantle into the geological past.

To address this shortcoming, a growing number of studies incorporate geochemical tracers, such as Nd isotopes, when modeling the mantle's evolutionary pathway over billions of years (e.g., Nakagawa et al., 2010; van Heck et al., 2016; Barry et al., 2017; R. E. Jones et al., 2019; T. D. Jones et al., 2021). This approach has been instrumental to our understanding of the development of present-day mantle structure, particularly formation of large-low-velocity zones at the base of the mantle. However, simulations of this nature can only investigate whole-mantle processes over Earth history. This starting point limits their ability to generate high-resolution simulations of short-lived geologic events. Moreover, like studies that rely on geophysical constraints, these isotopic simulations are validated using present-day observations of mantle structure. To determine whether geodynamical simulations accurately reproduce past mantle processes, they must compute predictions for a wider variety of geologic observations.

The composition of igneous rocks at Earth's surface acts as a permanent, albeit incomplete, record of melting within the mantle and, hence, can be used to inform simulations into the geologic past. Melting in the mantle is rare, and so simulations that predict the distribution and extent of melting, and compare these predictions to the spread of igneous rocks at the surface, can offer important insights into upper-mantle structure at mid-oceanic ridges (e.g., Keller et al., 2017; Sim et al., 2020), subduction zones (e.g., Perrin et al., 2018; Rees Jones et al., 2018), and intraplate settings (e.g., Lees et al., 2020; Duvernay et al., 2021). However, comparisons between calculated melt estimates and observed igneous-rock distributions are often imperfect since in many locations the majority of melt is trapped within the lithosphere (Crisp, 1984). The ability to predict melt chemistry within geodynamical simulations unlocks the full potential of igneous rocks to constrain upper-mantle processes through space and time (e.g., Watson & M^{c}Kenzie, 1991; Plank & Langmuir, 1992; Bown & White, 1994; Asimow & Langmuir, 2003; Gregg et al., 2009; Behn & Grove, 2015; Brown et al., 2020; Krein et al., 2020). To first order, incompatible-element compositions of mafic igneous rocks are analogous to those of primitive mantle melts, i.e., melts that have not undergone fractional crystallisation (Gast, 1968; Frey et al., 1974). Primitive melts commonly represent an accumulation of melts generated at a wide range of thermal, chemical, mineralogical and dynamical conditions (Langmuir et al., 1977). The volume and composition of each melt is sensitive to these conditions and, hence, aggregate primitive melts, and corollary igneous rocks observed at the surface, largely reflect the thermo-chemical and dynamical structure of the upper mantle (e.g., Klein & Langmuir, 1987; McKenzie & O'Nions, 1991; Niu et al., 2011; Dalton et al., 2014; Ball et al., 2021). By comparing computed melt compositions with observed igneous rock compositions, it is possible to test the veracity of geodynamical simulations through geologic time. Furthermore, integrating geochemical calculations within a geodynamical modeling framework provides a means to investigate how changes to upper-mantle thermo-chemical structure affect melt compositions.

In this study, we present a peridotite melting parameterization, BDD21, that calculates melt incompatible-element concentrations as a function of pressure, temperature, melt fraction and mantle composition. BDD21 is designed so that it can be integrated with a range of geodynamical codes that incorporate a tracer-particle functionality. It can therefore be used within geodynamical simulations over a wide range of geologic settings to predict melt incompatible-element compositions through space and time. Here, we demonstrate BDD21's functionality using the Fluidity computational modelling framework (e.g., Davies et al., 2011; Mathews, 2021).

To test the versatility of our approach, we apply our coupled Fluidity-BDD21 framework to two contrasting geologic settings: melting at mid-oceanic ridges and adjacent to step-changes in lithospheric thickness. At mid-oceanic ridges, extensive melt production occurs in response to passive upwelling generated by divergent plate velocities. If prescribed plate velocities, underlying mantle temperature, and mantle composition remain constant through time, upwelling rates and melting diagnostics will approach a steady-

state that persists for millions of years. As such, we are able to test the sensitivity of melt volume and melt composition to variables such as plate velocity, mantle temperature and mantle depletion. These predictions can subsequently be compared to global datasets from mid-oceanic ridges (e.g., Gale et al., 2013; Hoggard et al., 2017; Richards et al., 2020). At lithospheric steps, lateral density variations that accompany steep gradients in lithospheric thickness trigger small-scale convective flow (King & Anderson, 1998). This flow field changes over time, as the instabilities and overlying thermal boundary layer evolve. In contrast to mid-oceanic ridges, melting at lithospheric steps is deeper, less voluminous and ephemeral, as melting is inhibited by thickening of the overlying thermal-boundary layer (Duvernay et al., 2021). Since melt composition is strongly sensitive to the extent and depth of melting, applying BDD21 to these contrasting geologic settings allows us to demonstrate the sensitivity of melt composition to temperature, lithospheric thickness and mantle flow across different melting regimes. Therefore, integrating BDD21 into geodynamical simulations will help to reveal how the uppermost mantle's thermo-chemical structure and flow regime influence melt compositions observed at the surface through space and time.

2 Geodynamical Modeling Framework

In the upper-mantle convection simulations considered below, we solve the incompressible Stokes and energy equations relevant to mantle convection using Fluidity, a finite-element, control-volume computational modeling framework based upon adaptive, unstructured discretisations (Davies et al., 2011; Kramer et al., 2012, 2021). Our simulations are 2-D, and we focus upon melting at mid-oceanic ridges and lithospheric steps. Melting is tracked using the particle-in-cell method, with particles advected using a 4^{th}-order Runge-Kutta scheme. Further details on Fluidity and the implementation of its particle-in-cell scheme can be found in Davies et al. (2011) and Mathews (2021), respectively. Our melting and geochemical parameterizations are described below. Note that our simulations assume that the mantle is incompressible and, hence, temperature does not decrease adiabatically as particles ascend to shallower depths. Accordingly, when calculating melt productivity within this study, we assume that simulation mantle temperatures represent potential temperatures (T_p).

2.1 Melting Parameterization

Within our simulations, melt generation is governed by an adapted version of the hydrous lherzolite melting parameterization of Katz et al. (2003). Here, some of the material constants within this parameterization have been updated to honor experimental constraints that have subsequently been obtained (Supplementary Materials; Shorttle et al., 2014). Assuming that clinopyroxene remains present, or has already been exhausted during melting, melt productivity as the mantle decompresses is defined as

$$\left.\frac{dX}{dP}\right|_S = \frac{-\frac{C_P}{T}\left.\frac{dT}{dP}\right|_X + \frac{\alpha_s}{\rho_s} + X\left(\frac{\alpha_f}{\rho_f} - \frac{\alpha_s}{\rho_s}\right)}{\Delta S + \frac{C_P}{T}\left.\frac{dT}{dX}\right|_P}, \tag{1}$$

where P, T, X, S, ΔS, C_P represent pressure, temperature, melt fraction, entropy, entropy of fusion and specific heat capacity, respectively; the coefficient of thermal expansion and density are denoted by α and ρ, respectively; and subscripts s and f refer to the solid and fluid phases, respectively (McKenzie, 1984). This equation describes adiabatic decompression melting, and changes in temperature are tracked during melting

by integrating

$$\left.\frac{dT}{dP}\right|_S = T\left[\frac{\frac{\alpha_s}{\rho_s} + X\left(\frac{\alpha_f}{\rho_f} - \frac{\alpha_s}{\rho_s}\right) - \Delta S \left.\frac{dX}{dP}\right|_S}{C_P}\right], \tag{2}$$

simultaneously with Equation 1. Here, we adapt these equations to allow each particle to decompress along its respective temperature gradient calculated within each Fluidity simulation. We assume that

$$\frac{\alpha_s}{\rho_s} + X\left(\frac{\alpha_f}{\rho_f} - \frac{\alpha_s}{\rho_s}\right) \sim \frac{C_P}{T}\left.\frac{dT}{dP}\right|^{\text{Fluidity}}, \tag{3}$$

where the derivative super-script signals that this temperature gradient is sourced from Fluidity (for derivation of this relationship, see Supplementary Equation 3). Accordingly, by substituting Equation 3 into Equations 1 and 2 and rearranging, we obtain the following system of coupled equations:

$$\left.\frac{dX}{dP}\right|_S \sim \frac{\left.\frac{dT}{dP}\right|^{\text{Fluidity}} - \left.\frac{dT}{dP}\right|_X^{\text{Katz}}}{\frac{T\Delta S}{C_P} + \left.\frac{dT}{dX}\right|_P^{\text{Katz}}}, \tag{4}$$

$$\left.\frac{dT}{dP}\right|_S \sim \left.\frac{dT}{dP}\right|^{\text{Fluidity}} - \frac{T\Delta S}{C_P}\left.\frac{dX}{dP}\right|_S. \tag{5}$$

When a particle exceeds the solidus, Equations 4 and 5 are jointly integrated to calculate the evolution of melt fraction and temperature as a function of pressure. Each Lagrangian particle thus records a value of X at each time-step and stores the maximum value encountered throughout the simulation ($X_{\max}$). Melting occurs when the newly obtained X is higher than X_{max} and a melting rate (M) is subsequently calculated from the value of the time-step (δt) at this stage:

$$M = \max\left(0, \frac{X - X_{\max}}{\delta t}\right). \tag{6}$$

During melting, latent heat is consumed and, hence, temperatures decrease. These temperature variations are fed back into Fluidity through a source-term in the energy equation. For simplicity, we do not attempt to simulate melt extraction or melt refreezing.

2.2 Mid-Oceanic Ridge Simulation Set-Up

We simulate mantle flow beneath a mid-oceanic ridge in an idealised 2-D computational geometry (Figure 1a; Table A1). Our domain extends horizontally (x) for 990 km either side of the ridge axis and vertically (z) from the surface to 660 km depth. The upper boundary has an imposed horizontal velocity (v_x) which represents the motion of the oceanic plate; no vertical flow through this boundary is permitted. Plate velocity acts in opposite directions either side of the ridge, and so plate speed is equivalent to the half spreading rate (R_s). v_x is also prescribed at side boundaries and varies as a function of $1/z^2$ from $v_x = R_s$ at the surface to $v_x = 0$ at 660 km depth. The bottom boundary is open. Temperature boundary conditions are fixed to 0 °C at the surface of the simulation, a constant user-defined temperature (T) at the base, and zero heat flux boundary conditions on both sides. Initial conditions comprise a plate with an age increasing from the ridge (0 Myr at x=990 km) to the sides, following a half-space cooling model. Mesh spacing varies from ~ 0.5 km near the top boundaries to 70 km at the domain's base.

We consider a mantle undergoing deformation through a composite diffusion and dislocation creep (i.e. mixed) rheology. Viscosity (μ) is calculated at each time step from the general power law

$$\mu = A^{-\frac{1}{n}} \exp\left(\frac{E+PV}{nRT}\right)\dot{\epsilon}_{II}^{\frac{1-n}{n}}, \tag{7}$$

where $\dot{\epsilon}_{II}$ is the second invariant of the strain-rate tensor, n is the stress exponent that depends on the deformation mechanism, E and V are activation energy and volume, A is a pre-factor, $P = \rho g z$ is the lithostatic pressure, R is the gas constant and T is temperature. Note that the rheological parameters, detailed in Table A1, are chosen to yield realistic upper-mantle viscosity values that are consistent with geophysical constraints, following the methodology of Garel et al. (2014). These parameters are also compatible with experimental data (Hirth & Kohlstedt, 2003; Korenaga & Karato, 2008). The effective viscosity is calculated via a harmonic mean as $\left(\mu_{\text{diff}}^{-1}+\mu_{\text{disl}}^{-1}\right)^{-1}$ with μ_{diff} and μ_{disl} the viscosity associated to diffusion and dislocation creep, respectively.

Melting commences when mantle material reaches the peridotite solidus and ceases when this material no longer advects upwards or cools down to sub-solidus conditions. The occurrence of melting, and consequently the geometry of the melt region, is tracked by tracer particles. For our mid-oceanic ridge simulations, particles are randomly initialized at depths below the solidus over a wide region so that all possible melting paths are captured throughout each simulation. Diagnostics are analysed once each simulation has reached steady state.

2.3 Lithospheric Step Simulation Set-Up

The geodynamical set-up of our lithospheric step simulations is similar to the 2-D cases described in Duvernay et al. (2021). Key simulation parameters are summarised in Table A2. The modeling domain extends in the vertical direction (z) from the surface to 1000 km depth and horizontally (x) over 4000 km (Figure 1b). No external forcing is included within this simulation. Simulation boundaries are free-slip apart from the bottom boundary which is no-slip. The asthenospheric interior of these simulations have initial mantle temperatures of 1325 °C, while the surface temperature is set to 17 °C. No heat transfer is allowed through the sidewalls of the simulation.

Steps in lithospheric thickness are imposed over 200 km wide zones between a central region of thick continental lithosphere and surrounding thinner oceanic lithosphere. The continent lies between x = 1350–2650 km and has a thickness of 200 km, with the upper 41 km representing the crust. The initial temperature distribution within the continental interior follows a conductive geotherm obtained by solving the 1-D heat equation. For this calculation, we use a thermal conductivity of 3 $\text{Wm}^{-1}\text{K}^{-1}$ and internal heat generation with an exponential decrease of characteristic length scale 9 km (Lachenbruch, 1970; Schatz & Simmons, 1972; Pollack & Chapman, 1977). Either side of this continental core, the oceanic lithosphere is treated as a thermal-boundary layer with a temperature profile that adheres to a half-space cooling model.

We define viscosity (μ) through a diffusion creep rheology law

$$\mu = A \times \exp\left(\frac{E^* + \rho_0 g z\, V^*}{R(T+\psi z)}\right). \tag{8}$$

Viscosity is temperature- and depth-dependent. At 660 km depth, μ reaches a value of 10^{21} Pa·s in the upper mantle and jumps to a constant value of 2×10^{22} Pa·s in the underlying lower mantle. Within the continent, to ensure the stability and longevity of the lithospheric block, viscosity is increased by a factor of 100.

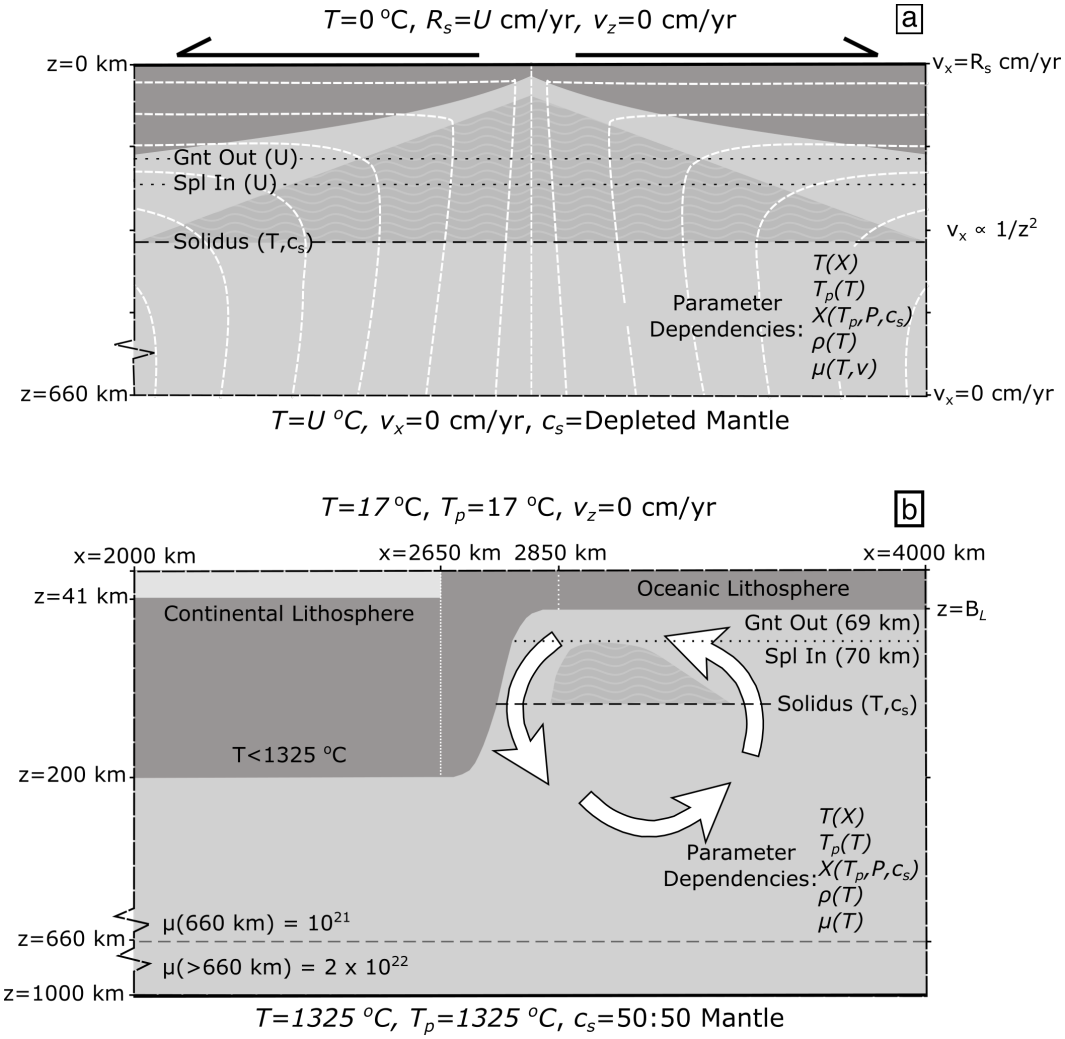

Figure 1. Schematic diagrams of geodynamical simulation domains with boundary conditions and parameter dependencies. a) Mid-oceanic ridge simulation illustrated with simplified representation of the thermal boundary layer (darkest grey), melting region (dark grey with wavy white lines) and mantle streamlines (dashed white lines). Bottom and side boundaries are open for normal flow. Text above and below simulation domain describe boundary conditions at $z = 0$ km and $z = 660$ km, respectively. U = User defined value. b) Same as panel a but for the lithospheric step case. Additional features include: continental crust (lightest grey); stylised mantle flow lines (white arrows); B_L = oceanic thermal boundary layer thickness at time = 0 Myr. Dashed boundaries = free-slip, solid boundary = no-slip. Simulation domain mirrored along left-hand side.

Our mid-oceanic-ridge simulations are analysed once they achieve steady state and particles are present throughout the melt region. In the lithospheric step case, we are interested in the spatio-temporal melting trends as these simulations do not approach a steady-state melting regime. Therefore, our lithospheric step simulations are initialized with particles distributed across the entire computational domain. Particles initialized at supra-solidus conditions are assigned initial melt fractions assuming that they underwent instantaneous melting at that depth.

3 Geochemical Melting Parameterization

Our geodynamical modeling framework provides a means to compute the spatio-temporal evolution of the upper mantle's structure, flow regime and associated melt distribution. To generate melt compositions that can be compared to the composition of mafic igneous rocks erupted at Earth's surface, a geochemical melting parameterization must be integrated into our geodynamical framework. Our geochemical melting parameterization is similar to those of Kimura and Kawabata (2014) and Brown and Lesher (2016), which exploit peridotite melting experiments to parameterize mineralogy and melt stoichiometry throughout the mantle (Baker & Stolper, 1994; Walter, 1998; Falloon et al., 1999). This approach represents an improvement on earlier parameterizations that were developed prior to these experiments being conducted (e.g., McKenzie & O'Nions, 1991; Langmuir et al., 1992). It is less computationally expensive than sophisticated thermodynamically-consistent parameterizations (e.g., Ghiorso et al., 2002; Connolly, 2005; Holland et al., 2018) and, thus, is very-well suited for integration within geodynamical simulations. Our approach is different to some previous coupled geochemical-geodynamical melting schemes (e.g., Behn & Grove, 2015; Krein et al., 2020). These schemes primarily focused on major element systems, and so they parameterize the equilibrated composition of the melt rather than the mineralogy of the source (Till et al., 2012). Here, we describe BDD21, a Python package for calculating incompatible element concentrations within melts as a function of pressure, temperature, melt fraction and mantle composition.

3.1 Fractional Melting Functions

The concentration of an incompatible element within an instantaneous melt (c_l) and the concentration of that element within the residue (c_s) are related to each other by two equations that must be simultaneously solved (White et al., 1992). These equations are

$$\frac{dc_s}{dX} = \frac{c_s - c_l}{1 - X} \quad \text{and} \quad c_l = \frac{c_s(1 - X)}{\bar{D} - \bar{P}X}, \tag{9}$$

where X is the melt fraction, and where $\bar{D}$ and $\bar{P}$ are the bulk distribution coefficients for a given element within the solid assemblage and the melting assemblage, respectively (Shaw, 1970).

To calculate c_l and c_s for a given particle, these equations are numerically integrated using the LSODA algorithm (Hindmarsh, 1983; Petzold, 1983) from the solidus, where $X = 0$, to the particle's present location, where $X = X'$. The path between these limits for each particle, $X(P, T)$, is dictated by the flow field of our geodynamical simulations (Section 2).

Together, $\bar{D}$ and $\bar{P}$ determine how readily an incompatible element will partition into the melt. $\bar{D}$ and $\bar{P}$ are the sum of the distribution coefficients for each mineral phase, D_{mnl}, scaled by their modal abundance in the solid and liquid phase, respectively. Therefore,

$$\bar{D} = \sum_{n=1}^{N} F_{mnl} D_{mnl} \quad \text{and} \quad \bar{P} = \sum_{n=1}^{N} p_{mnl} D_{mnl}, \tag{10}$$

where N is the total number mineral phases present, F_{mnl} is the modal abundance of a mineral, and p_{mnl} is linked to the change in F_{mnl} at each melting step, as follows:

$$\sum_{n=1}^{N} F_{mnl} = 1 \quad \text{and} \quad p_{mnl} = F_{mnl} - (1 - X)\frac{dF_{mnl}}{dX} \tag{11}$$

(Shaw, 1979). $\bar{D}$ and $\bar{P}$ vary as a function of depth since the mineral assemblage, melt stoichiometry, and compatibility of an element within each mineral are pressure and melt-fraction dependent. In the following sections, we parameterize each of these variables within our geochemical framework.

3.2 Mantle Modal Mineralogy and Melting Reaction Stoichiometry

Peridotite melting experiments can be utilised to develop a simple parameterization of mantle mineralogy as a function of pressure and melt fraction. Along similar lines to recent geochemical parameterizations (e.g., Kimura & Kawabata, 2014; Brown & Lesher, 2016), we exploit experimental studies that record mineral abundances as a function of

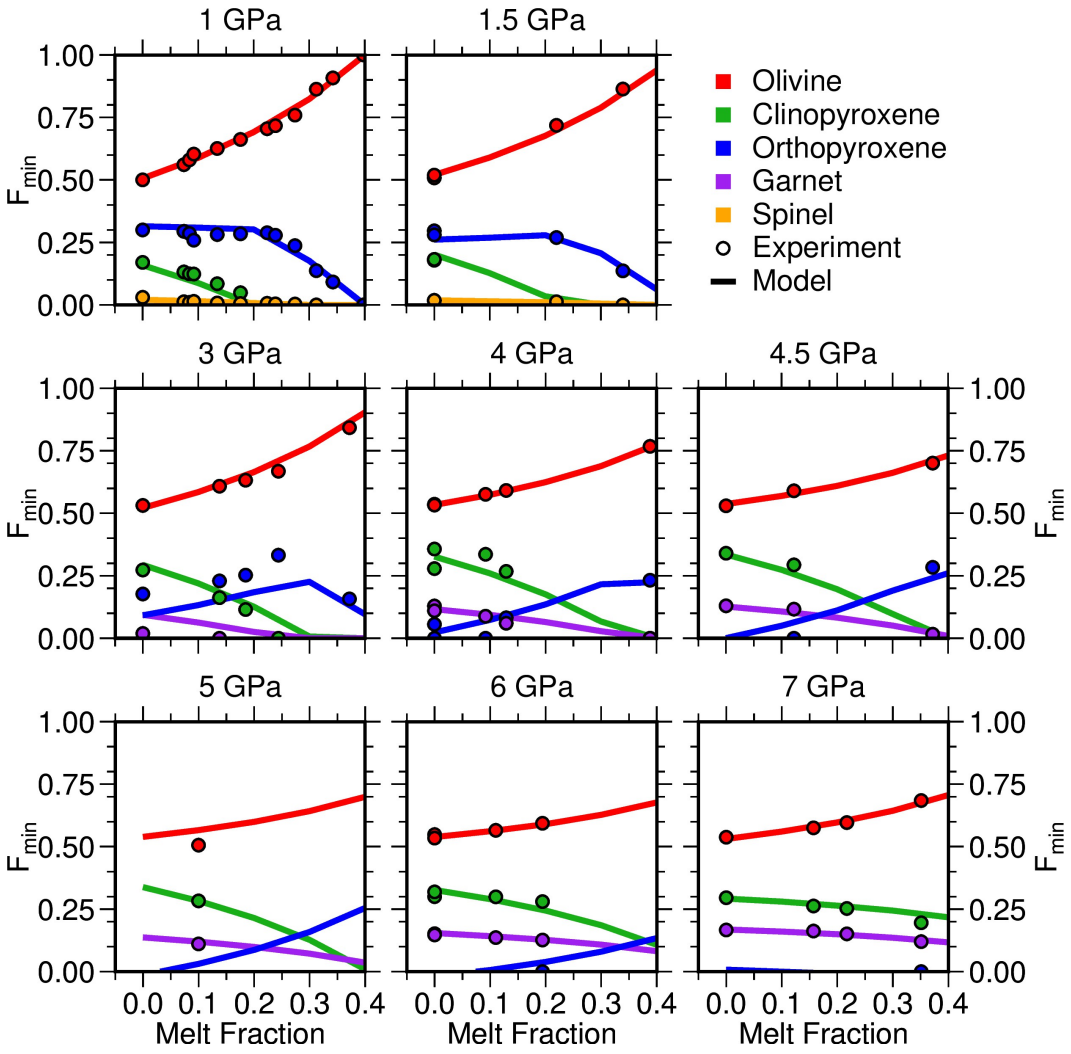

Figure 2. Modal mineralogy as a function of melt fraction at a range of pressures. Red, blue, green, purple and orange circles represent experimental modal proportions of olivine, orthopyroxene, clinopyroxene, garnet and spinel, respectively (Baker & Stolper, 1994; Walter, 1998; Falloon et al., 1999). Colored lines = parameterized proportions of each mineral as a function of melt fraction using Equations 12, 13 and 15. Note that experiments conducted at 3 and 5 GPa were not used to predict modal mineralogy.

melt fraction for the MM3 and KR4003 lherzolites at 1–1.5 and 3–7 GPa, respectively (Baker & Stolper, 1994; Walter, 1998; Falloon et al., 1999). We assume that these experimental results can be combined since these lherzolites have similar major element compositions (Kimura & Kawabata, 2014). Four mineral phases exist within these lherzolites: olivine (ol), orthopyroxene (opx), clinopyroxene (cpx) and an aluminous phase. The aluminous phase present varies as a function of depth between plagioclase, spinel (spl) and garnet (gnt). Plagioclase is stable within the mantle at pressures $\lesssim 1$ GPa (Borghini et al., 2010). At ambient mantle temperatures, once the mantle has decompressed to $\sim$ 1 GPa, melt fractions are sufficiently high such that plagioclase is commonly exhausted. Accordingly, and for simplicity, at this stage BDD21 does not include a parameterization for melting within the plagioclase-stability field: any experiment where plagioclase exists as a stable phase is excised from our experimental database. We also remove experiments with > 20 % melting at depths ≥ 6 GPa since these conditions are unlikely to occur within the mantle.

At constant pressure (P), modal abundances for most minerals within these experiments vary approximately linearly as a function of X (if X is included as a modal phase, i.e., if all mineral phases sum to $1 - X$; Figure 2). Here, to parameterize $F_{mnl}(P, X)$ for olivine, clinopyroxene, garnet and spinel, we perform linear regressions through these data at constant pressure:

$$F_{mnl}(1 - X) = a_{mnl}X + b_{mnl}. \tag{12}$$

The empirically determined constants, a_{mnl} and b_{mnl}, from each linear regression at each pressure are then combined to parameterize $F_{mnl}(P, X)$ via a second-order polynomial regression:

$$a_{mnl} = a_0 + a_1P + a_2P^2 \quad \text{and} \quad b_{mnl} = b_0 + b_1P + b_2P^2. \tag{13}$$

At depths between $\sim$ 60–90 km, the stable aluminous phase changes from spinel to garnet through the following reaction:

$$\text{pyrope (gnt)} + \text{forsterite (ol)} \rightarrow 2 \times \text{enstatite (opx)} + \text{spinel}. \tag{14}$$

When performing polynomial regressions from 1–7 GPa, the proportion of garnet present at the solidus (i.e., F_{gnt} when $X = 0$), approaches zero at $\sim$ 2.7 GPa. The pressure range over which the spinel-garnet transition occurs is controversial: thermodynamical models typically place this transition at lower pressures than it occurs at within peridotite melting experiments (Green et al., 2012). Since partitioning of trace elements, especially heavy rare earth elements, is strongly dependent on the presence of garnet, we allow the depth of the spinel-garnet-transition zone to be a user-defined variable within our parameterization. We therefore calculate the modal mineralogy constants (a_{0-2} and b_{0-2}) for spinel- and garnet-bearing peridotite separately using experiments between 1–1.5 GPa and 4–7 GPa, respectively. All experiments from 1–7 GPa are used to calibrate $F_{cpx}(P, X)$ since clinopyroxene is not precipitated or consumed at this phase boundary. We assume that mantle modal mineralogy varies linearly between the mineral assemblages estimated to be present at the top and bottom of the spinel-garnet-transition zone.

The proportion of orthopyroxene present in the mantle (F_{opx}) does not vary linearly as a function of melt fraction, since it strongly depends on whether clinopyroxene is a stable phase (Figure 2). For simplicity, we assume that F_{opx} accounts for the total missing fraction when all other mineral contributions are combined:

$$F_{opx} = 1 - F_{ol} - F_{cpx} - F_{spl} - F_{gnt}. \tag{15}$$

Our empirically determined modal mineralogy constants are listed in Table 1. The fit between these parameterizations and the experimental data can be seen in Figure 2. Note that, with the exception of clinopyroxene, experiments performed at 3 GPa are not exploited to calibrate $F_{mnl}(P, X)$ since these experiments occur close to the spinel-garnet transition zone. The single experiment conducted at 5 GPa is excluded since a linear regression cannot be performed on one data point.

3.3 Mineral Distribution Coefficients

To calculate bulk distribution coefficients, the partition coefficients between each mineral and the melt phase (D_{mnl}) must be parameterized. A notable difference between BDD21 and those of similar melting parameterizations (e.g., Kimura & Kawabata, 2014; Brown & Lesher, 2016) is that, where possible, we estimate partition coefficients as a function of pressure, temperature and composition using a lattice strain equation (Brice, 1975). The compatibility of an element within a mineral is principally controlled by the valency of the element and the size difference between the element and the mineral host site. Isovalent cations in minerals can be described using the same lattice strain equation, where D_{mnl} depends on three material properties: the radius of the site (r_o), the elastic response of the site (E_M) and the partition coefficient for an ideal element with a radius of r_o, (D_o; Brice, 1975). These material properties vary as a function of pressure (P), temperature (T) and mineral major-element chemistry (χ) since changes in these variables cause sites within mineral lattices to expand and contract (Brice, 1975). As such, to use this lattice strain equation to define $D_{mnl}(P, T, \chi)$ for each cation site within each mineral, we must parameterize $r_o(P, T, \chi)$, $E_M(P, T, \chi)$ and $D_i(P, T, \chi)$. Mineral-melt partitioning experiments at a range of thermochemical conditions can be exploited to empirically estimate r_o, E_M and D_i as a function of P, T and χ (Wood & Blundy, 1997). Chosen lattice strain parameterizations used within BDD21 are shown in Table 2. For some cation valency-mineral pairs, $D_{mnl}(P, T, \chi)$ is less well constrained and so in these cases we assume D_{mnl} is invariant (Supplementary Table 1; McKenzie & O'Nions, 1995). For a full description of how we parameterize $D_{mnl}(P, T, \chi)$ for each element, see Supplementary Information (Shannon, 1976; Wood & Banno, 1973; Hazen & Finger, 1979; Landwehr et al., 2001; Blundy & Wood, 2003; Hill et al., 2011).

3.4 Mantle Composition

The experiments used to parameterize mantle mineralogy during melting were conducted using lherzolites that are assumed to represent primitive mantle (PM). However, more refractory sources, such as depleted MORB mantle (DMM), may also be present during melting. For melting of DMM, we adopt the same approach as Kimura and Kawa-

Table 1. Constants for calculating modal mineralogy as a function of melt fraction in Equations 12 and 13.

Spinel Peridotite	a_0	a_1	a_2	b_0	b_1	b_2
F_{ol}	0.318	0.314	−0.115	0.419	0.126	−0.039
F_{cpx}	−0.606	−0.229	0.037	0.058	0.112	−0.011
F_{spl}	−0.087	−0.013	0.026	0.020	0.004	−0.004
Garnet Peridotite	a_0	a_1	a_2	b_0	b_1	b_2
F_{ol}	1.298	−0.558	0.048	0.445	0.035	−0.003
F_{cpx}	−0.606	−0.229	0.037	0.058	0.112	−0.011
F_{gnt}	−0.557	0.078	−0.005	0.008	0.033	−0.001

bata (2014), increasing F_{ol} by 0.04 at the expense of F_{cpx}. Note that when clinopyroxene is exhausted, or close to exhaustion, this reduction in F_{cpx} is accommodated via a complementary reduction in F_{opx}, ensuring that Equation 15 remains satisfied. When a combination of PM and DMM is used, this change to modal mineralogy is scaled linearly according to the proportions of PM and DMM in the source (e.g., for a mantle of 50% PM and 50% DMM, F_{ol} and F_{cpx} are increased and reduced by 0.02, respectively). Concentrations of incompatible elements within the source region prior to melt initiation are also linearly varied between the primitive and depleted compositions of McDonough and Sun (1995) and Salters and Stracke (2004), respectively. In the primitive case, H_2O concentration is set to 280 ppm based on the assumption that the concentration of H_2O is 200× greater than that of Ce (Michael, 1995). The concentration of water in depleted mantle is set to 100 ppm (Salters & Stracke, 2004).

3.5 Application to a One-Dimensional Melting Column

Before applying BDD21 to 2-D geodynamical simulations, we first describe how mantle mineralogy and melt composition respond to isentropic melting in a simple 1-D case. A particle of primitive mantle with $T_p = 1325$ °C ascends vertically from 3.5 GPa to the surface. As this particle rises, it intersects the solidus at ~ 100 km depth and begins to melt (Figure 3a). Melt productivity increases as X increases, and so the first few degrees of melting happen over a larger depth interval (Figure 3b; Katz et al., 2003). These initial melts are generated in the garnet stability field through the consumption of clinopyroxene, garnet and small amounts of olivine, and the precipitation of orthopyroxene (Figure 3c–f). For this illustrative example, we have placed the spinel-garnet transition at 69–70 km depth (Jennings & Holland, 2015). Both the mantle mineralogy and melting reaction stoichiometry are radically altered as the spinel-garnet-transition zone is crossed. At the transition zone, garnet and olivine react to form orthopyroxene and spinel (Equation 14). Beyond this boundary, clinopyroxene is consumed and olivine is precipitated during melting. At shallow depths olivine begins to be consumed and orthopyroxene is precipitated, with the importance of this reaction increasing once clinopyroxene has been exhausted.

As elements vary in abundance and compatibility, each element behaves differently during melting. Of the major mineral phases present in the mantle, Na is most compatible within clinopyroxene and the compatibility of Na within clinopyroxene increases as a function of pressure (Blundy et al., 1995). As the particle decompresses and melts, clinopyroxene is consumed and Na becomes increasingly incompatible within the solid phase. Therefore, an increase in instantaneous melt Na concentrations is observed between the

Table 2. Incompatible element partitioning parameterizations for each mineral as a function of element valency. All other mineral-elements partition coefficients treated as constant values (Supplementary Table 1; McKenzie & O'Nions, 1995).

Mineral	Parameterisation	Mineral	Parameterisation
Olivine		**Orthopyroxene**	
3+	Sun and Liang (2013)	2+	Wood and Blundy (2014)
		3+	Yao et al. (2012)
Clinopyroxene			
1+	Wood and Blundy (2014)	**Garnet**	
2+	Wood and Blundy (2014)	3+	Sun and Liang (2013)
3+	Sun and Liang (2012)	4+	Mallmann and O'Neill (2007)
4+	Wood and Blundy (2014)		

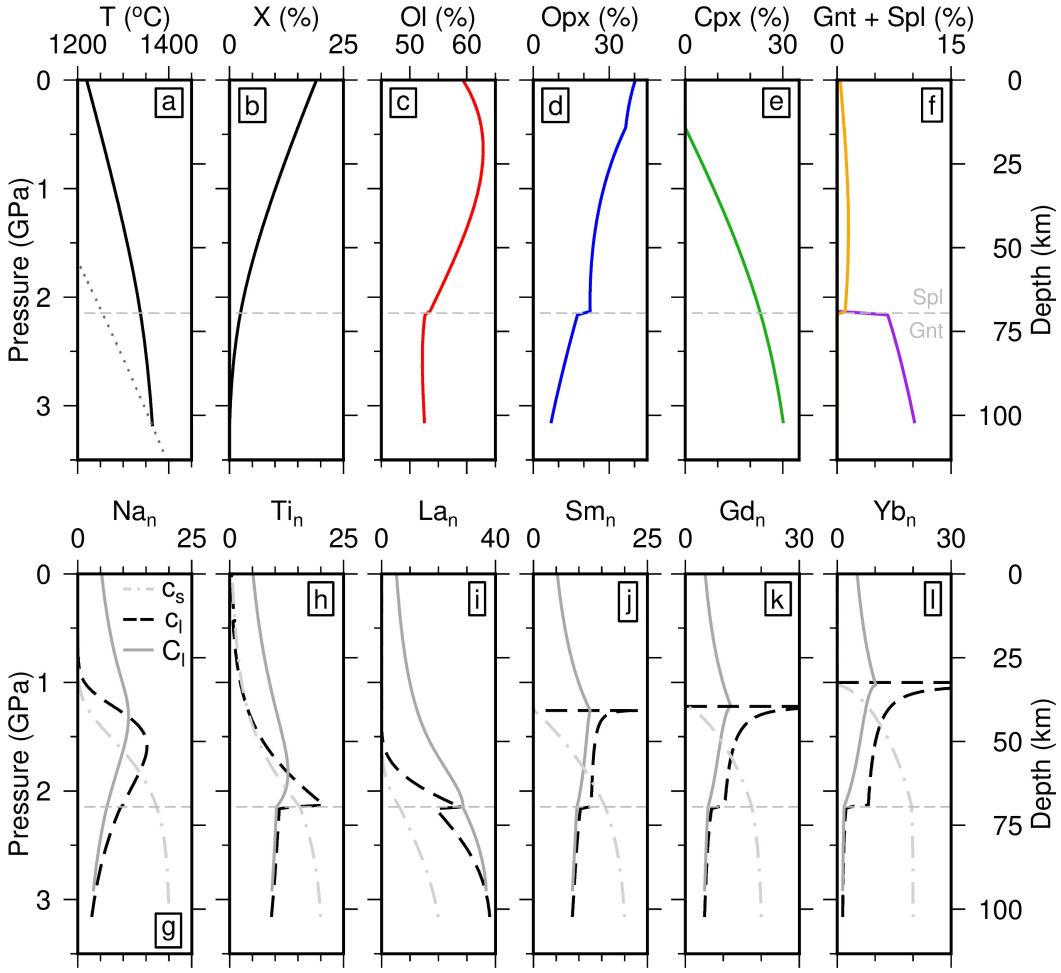

Figure 3. 1-D isentropic decompression melting of a particle of primitive mantle at T_p = 1325 °C. a) Temperature as a function of pressure. Solid line = prediction from melt parameterization, dotted grey line = solidus, dashed gray lines = spinel-garnet-transition zone. b) melt fraction (X). c–f) percentage abundance of each mineral; purple and orange lines represent garnet and spinel abundances, respectively. g–l) Concentration of each element normalised by initial source concentration (McDonough & Sun, 1995). Solid / dashed / dot-dashed lines = C_l / c_l / c_s normalised by source composition. Note that, for illustrative purposes, c_s values have been increased by a factor of 20.

solidus and ∼ 1.5 GPa (Figure 3g). Beyond ∼ 1.5 GPa, the concentration of Na in the instantaneous melt decreases.

The compatibility of many elements changes considerably at the spinel-garnet transition zone. Ti is less compatible within spinel peridotite than within garnet peridotite, and so once this threshold is exceeded the concentration of Ti within the instantaneous liquid sharply increases (Figure 3h). The concentration of highly incompatible elements entering the melt decreases and melting continues as these elements become less abundant within the source. Light rare earth elements, such as La, are highly incompatible in garnet peridotite and, accordingly, concentrations of these elements within the liquid rapidly decrease as a function of melt fraction (Figure 3i). Note that, for un-normalised

concentrations, the gradient of this decrease is a function of both the incompatibility of the element and its concentration in the residue. Heavier rare earth elements, such as Sm, Gd and Yb, are more compatible in garnet peridotite than spinel peridotite. Therefore, the concentrations of these elements in the instantaneous melts increase when the spinel-garnet transition zone is exceeded (Figure 3j-l). Between the spinel-garnet transition zone and $\sim$ 25 km depth, clinopyroxene and olivine are consumed and precipitated, respectively. Therefore, heavy rare earth elements become increasingly incompatible in the solid phase and preferentially enter the melt phase until they are exhausted. Since the integrated melt composition (C_l) is a weighted sum of all instantaneous (c_l) generated thus-far,

$$C_l = \frac{1}{X_{\max}} \int_0^{X_{\max}} c_l(X)\, dX, \tag{16}$$

C_l changes at a slower rate than c_l. After each element in exhausted, they no longer enter the instantaneous melt phase and so their concentrations in the integrated liquid composition decrease as melting continues.

4 Application to Mid-Oceanic Ridges

Using BDD21 and Fluidity, we have constructed a coupled geochemical-geodynamical computational modeling framework of steady-state mid-oceanic spreading centres, at a range of different mantle potential temperatures, plate spreading rates and source compositions. To validate these mid-oceanic ridge simulations and, therefore, our overall approach, we next compare the predictions from our simulations with a suite of geological observations.

To compare our simulation predictions to observations, crustal thickness and melt composition must be calculated for each simulation. Melt production beneath mid-oceanic ridges can extend for $>$ 100 km either side of the ridge axis (Forsyth et al., 1998). To form oceanic crust, melts must travel laterally towards the ridge axis. Generally, melts that migrate greater lateral distances are more likely to refreeze within the lithosphere and are, therefore, less likely to contribute to oceanic crust formation (Plank & Langmuir, 1992; Katz, 2008; Keller et al., 2017; Sim et al., 2020). We do not attempt to model complex melt extraction and refreezing processes. Instead, we rely on simple relationships observed by Keller et al. (2017) within their mid-oceanic ridge melt extraction simulations. Keller et al. (2017) suggest that the passive focusing distance (x_f), i.e., the furthest lateral distance that melts can travel to ridge axis without freezing, is a function of upwelling velocity (v_y) and temperature, finding that x_f approximately coincides with the intersection between the isopleth that defines $v_z = R_s/3$ and the anhydrous peridotite solidus. We assume that all melts generated beyond these limits freeze within the lithosphere. Thus, the thickness of crust produced at the ridge axis (t_c) is calculated by

$$t_c = \frac{1}{2R_s} \frac{\rho_s}{\rho_c} \int_A M dA, \tag{17}$$

where M and A correspond to the the melting rate and melting region over which melt reaches the ridge axis, respectively(Forsyth, 1993). We assume that the density of oceanic crust (ρ_c) is 2900 kg m^{-3}.

Melt compositions are calculated once melting diagnostics (i.e., F and M) within the simulation reach a steady state. For the majority of these calculations, we assume that the mantle source is depleted (see Section 3.4; Salters & Stracke, 2004). We impose the spinel-garnet transition zone between 69–70 km depth (Jennings & Holland, 2015). Observations of radiometric isotopic systems at mid-oceanic ridges demonstrate that melts ascend through the mantle at velocities of order 10–100s m yr^{-1} (Stracke et al., 2006).

At these speeds, melts reach the ridge 10^3–10^5 yrs after inception. Given that these timescales are much shorter than those associated with mantle flow, we can assume that all melts generated within the magmatic focussing area (A), regardless of depth, are instantaneously extracted at the ridge axis. More productive regions of the simulation will contribute higher volumes of melt to the ridge axis. To account for these variations in productivity, when calculating the average composition of this pooled melt (C_l), we weight each instantaneous melt generated within the melt zone by its corresponding melt rate:

$$C_l = \frac{\int_A c_l M \, dA}{\int_A M \, dA}. \tag{18}$$

Crustal thicknesses and melt compositions calculated by our mid-oceanic ridge simulation are a function of mantle T_p, R_s, mantle composition, and the depth of the spinel-garnet transition zone. We systematically vary these parameters and compare our crustal thickness and melt composition predictions to global databases of mid-oceanic ridge observations.

4.1 Effect of Potential Temperature on Melting

In Figure 4, T_p is varied in 50 °C increments between 1275–1475 °C and R_s is held constant at 2.1 cm yr^{-1}. Increasing T_p displaces the solidus to greater depth, which causes the melt region to expand and higher melt fractions to be attained (McKenzie & Bickle, 1988, Figure 4a–c). Additionally, since the effective viscosity is inversely proportional to temperature, increasing T_p from 1275 °C to 1475 °C results in concomitant increases in upwelling and melting rates (1.96–2.34 cm yr^{-1} and 0.034–0.073 Myr^{-1} at 1.5 GPa beneath the ridge axis, respectively). The combined effects of a deeper solidus and increased upwelling rates widen the magmatic focusing distance (x_f) and supply a greater volume of melt to the ridge axis. As a result, we find that calculated crustal thicknesses increase from $3.19 - 14.94$ km as T_p increases from $1275 - 1475$ °C (Figure 4g).

We compare our results to a compilation of oceanic plate crustal thickness estimates derived from seismic velocity profiles (Hoggard et al., 2017). Where these estimates occur on crust < 3 Ma, we assign these crustal thickness values to their corresponding ridge segment (78 locations world-wide; Figure 5a). Potential temperatures for each ridge segment are estimated using a global parameterization of mantle T_p at 150±25 km depth calculated by converting the SL2013sv shear-wave tomographic model to temperature by fitting upper mantle seismic observations beneath the oceans to a plate model (Figure 5a; Schaeffer & Lebedev, 2013; Richards et al., 2020). Corresponding spreading rates for each ridge segment are taken from a global database (Gale et al., 2013). These rates are based upon established estimates of present-day absolute plate motion (NUVEL-1A and NNR-MORVEL56; Figure 5b; DeMets et al., 1994; Argus et al., 2011). Since our simulations are generated with a constant half-spreading rate of 2.1 cm yr^{-1}, results are only compared to crustal thickness values from ridges where $R_s = 2.1 \pm 1$ cm yr^{-1}. We find that crustal thickness estimates from our simulations are more sensitive to variations in T_p than crustal thicknesses measured at present-day mid-oceanic ridges (Figure 4g). For example, our simulations predict a crustal thickness of 8.68 km at a T_p of 1375 °C, whereas potential temperatures are estimated to be ~ 100 °C hotter under modern-day ridges with similar crustal thicknesses (Figure 4g).

Na_2O concentration is among the most-commonly used geochemical metrics at mid-oceanic ridges (e.g., Klein & Langmuir, 1987). As demonstrated in Section 3.5, Na becomes more compatible within clinopyroxene as depth increases (Figure 3; Blundy et al., 1995). Therefore, as T_p increases and the solidus deepens, Na_2O concentrations within the first melts formed decrease (Figure 4d–f). We find that simulations with elevated potential temperatures generate greater melt fractions over deeper melting columns, and consequently supply melts with lower Na_2O concentrations to the ridge axis. In Figure 4h, our Na_2O results are compared to the average Na_{90} value (i.e., Na_2O concentrations

corrected for the effects of fractionation so that the melt is in equilibrium with 0.9 Mg# olivine) recorded for basalts within each ridge segment (Figure 5b; Gale et al., 2014). Assuming that this correction is appropriate, our predictions of Na_2O concentrations should therefore be comparable to Na_{90} values. Again, we filter this database to only show Na_{90} values for ridges where $R_s = 2.1 \pm 1$ cm yr^{-1} and compare these values to T_p estimates at 150 ± 25 km depth (Richards et al., 2020). Observed Na_{90} concentrations decrease as potential temperatures increase up to ~ 1400 °C. At ~ 1400 °C, there is a break in slope and Na_{90} values decrease at a slower rate as T_p approaches 1500 °C. Our results closely match observed Na_{90} concentrations at potential temperatures < 1400 °C, although they do not fully-replicate the observed break in slope between Na_{90} and T_p. Instead, our simulations with $T_p > 1400$ °C slightly underestimate observed Na_{90} values.

The hypothesis that Na_2O concentrations in mid-oceanic ridge basalts are inversely proportional to mantle temperature variations is well established (e.g., Klein & Langmuir, 1987; Langmuir et al., 1992; Plank & Langmuir, 1992; Gale et al., 2013; Dalton et al., 2014). However, some authors argue that shallow magma chamber processes and mantle compositional heterogeneity, rather than T_p, are the primary drivers of geochemical variability in mid-oceanic ridge basalts (e.g., O'Hara, 1977, 1985; Niu & O'Hara, 2008; O'Neill & Jenner, 2012; Niu, 2016; O'Neill & Jenner, 2016). These studies highlight that correcting Na_2O concentrations back to Na_{90} values is difficult since Na is compatible in plagioclase and magma chambers are constantly replenished by primitive melts.

One way to avoid the pitfalls of conducting a fractional crystallisation correction is to employ incompatible element ratios. The geochemical ratio 10^4(Sm+Gd)/Ti is thought to be largely unaffected by fractional crystallisation and is observed to be almost constant throughout the mid-oceanic ridge system (8.61 ± 0.47; O'Neill & Jenner, 2016). Sm and Gd are far more compatible in clinopyroxene than in orthopyroxene, whereas the compatibility of Ti is more evenly spread between the two (Supplementary Table 1). Given this assumption, as clinopyroxene is consumed during partial melting, O'Neill and Jenner (2016) predicts that the 10^4(Sm+Gd)/Ti value of the melt should rapidly decrease. Given that this trend is not observed, O'Neill and Jenner (2016) infer that melt fractions do not vary significantly beneath mid-oceanic ridges (Figure 4i).

Within our simulations, however, we find that 10^4(Sm+Gd)/Ti increases as a function of melt fraction until Gd and Sm are exhausted, at which point the ratio becomes zero (Figure 4d–f). This difference between our predictions and those of O'Neill and Jenner (2016) arise since the relative abundances of clinopyroxene and orthopyroxene in the residue and entering the instantaneous melt are also a function of depth (Figure 2). By the time melt fractions reach $\sim 15\%$, Sm, Gd, and Ti are almost exhausted in the mantle and so the 10^4(Sm+Gd)/Ti value of the integrated melt at the ridge axis is approximately equal to that of the original source (8.33; Figure 4i; Salters & Stracke, 2004). Consequently, we recover 10^4(Sm+Gd)/Ti values within error of the global average at a range of T_p values (Figure 4h). Our results suggest that the limited spread of 10^4(Sm+Gd)/Ti values cannot be used as evidence that primitive melt compositions, and therefore cumulative melt fractions, are approximately uniform beneath the global mid-oceanic ridge system. We note that the upper flanks of our melting region record high Na_2O and 10^4(Sm+Gd)/Ti values. These high values arise from low melt productivity at the margins of the simulation and, as such, have a negligible influence on our predicted melt compositions, since they are down-weighted in our calculations (Equation 18).

4.2 The Effect of Spreading Rate on Melting

To generate the mid-oceanic ridge cases shown in Figure 6, we keep T_p fixed at 1325 °C and vary half-spreading rate (R_s) between 0.5–10 cm yr^{-1}. At slow spreading rates, passive upwelling speeds, and therefore melting rates, are substantially reduced. Mantle ascending at slower speeds is subjected to more extensive conductive cooling from the sur-

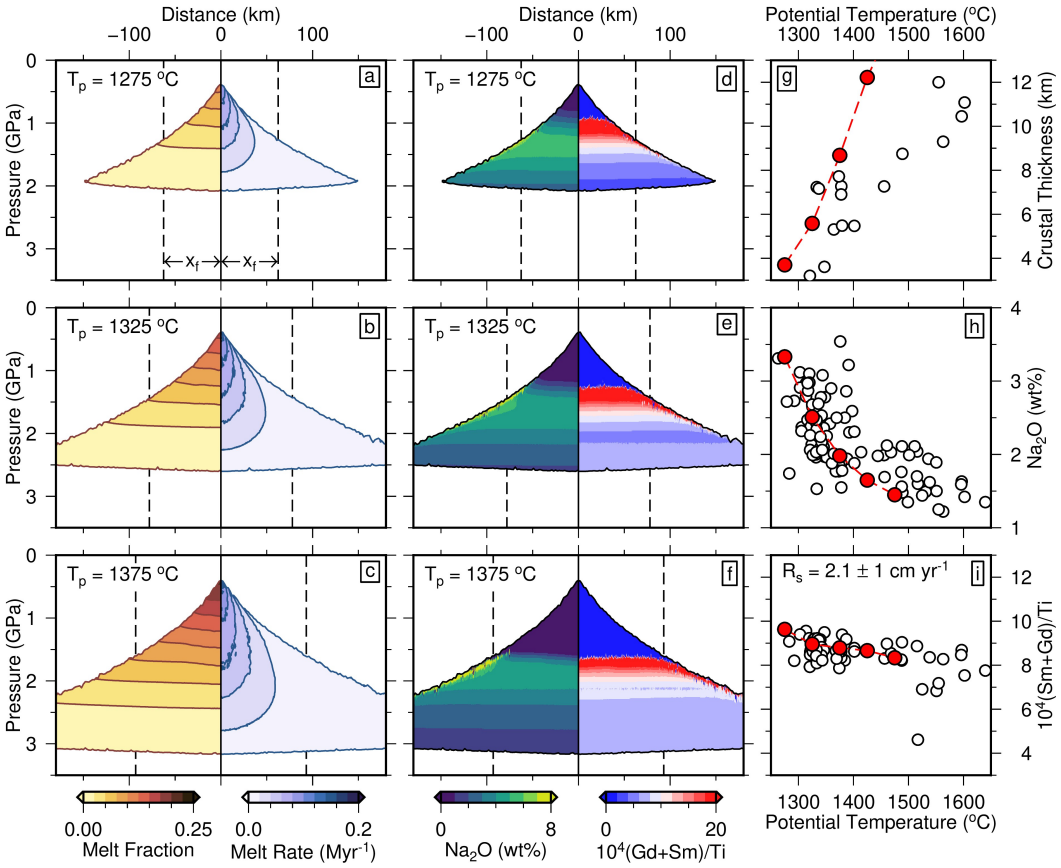

Figure 4. Melt region geometry at mid-oceanic ridges as a function of mantle temperature. a) Ridge-centered simulation with left- and right-hand sides coloured by melt fraction and melting rate, respectively. Simulation run with a potential temperature, T_p, of 1275 °C and a half-spreading rate, R_s, of 2.1 cm yr^{-1}. b–c) Same as panel a but with different T_p as indicated in top left corner of each panel. d) Same as panel a but left- and right-hand sides coloured by Na_2O concentration and 10^4(Sm+Gd)/Ti within the instantaneous melt phase, respectively. e–f) Same as panel d but with different T_p as indicated in top left corner of each panel. g) Crustal thickness as function of T_p. Red circles and dashed lines = calculated crustal thicknesses from cases shown in panels a–c and Supplementary Figure 7b,e; white circles = observed crustal thicknesses at mid-oceanic ridge segments with $R_s = 2.1 \pm 1$ cm yr^{-1} (Gale et al., 2013; Hoggard et al., 2017; Richards et al., 2020). h) Same as panel g with predicted Na_2O concentrations compared to estimated Na_{90} values at each ridge segment (Gale et al., 2013, 2014; Richards et al., 2020). i) Same as panel g with predictions compared to average 10^4(Sm+Gd)/Ti values at each ridge calculated using samples with MgO > 8.5 wt% (Gale et al., 2013; Richards et al., 2020).

face, which increases effective viscosity, further decreasing upwelling rates and, thus, causing melting to cease at greater depths.

In our simulations, these effects are particularly pronounced at $R_s < 2.1$ cm yr^{-1}. When $R_s \geq 2.1$ cm yr^{-1}, conductive cooling is reduced and maximum melt fraction and melting rates, in addition to crustal thickness, increase significantly (Figures 6a–c). However, as R_s increases beyond 2.1 cm yr^{-1} we observe a narrowing in the melt focusing distance, x_f, and a gradual reduction in crustal thickness estimates. This pattern

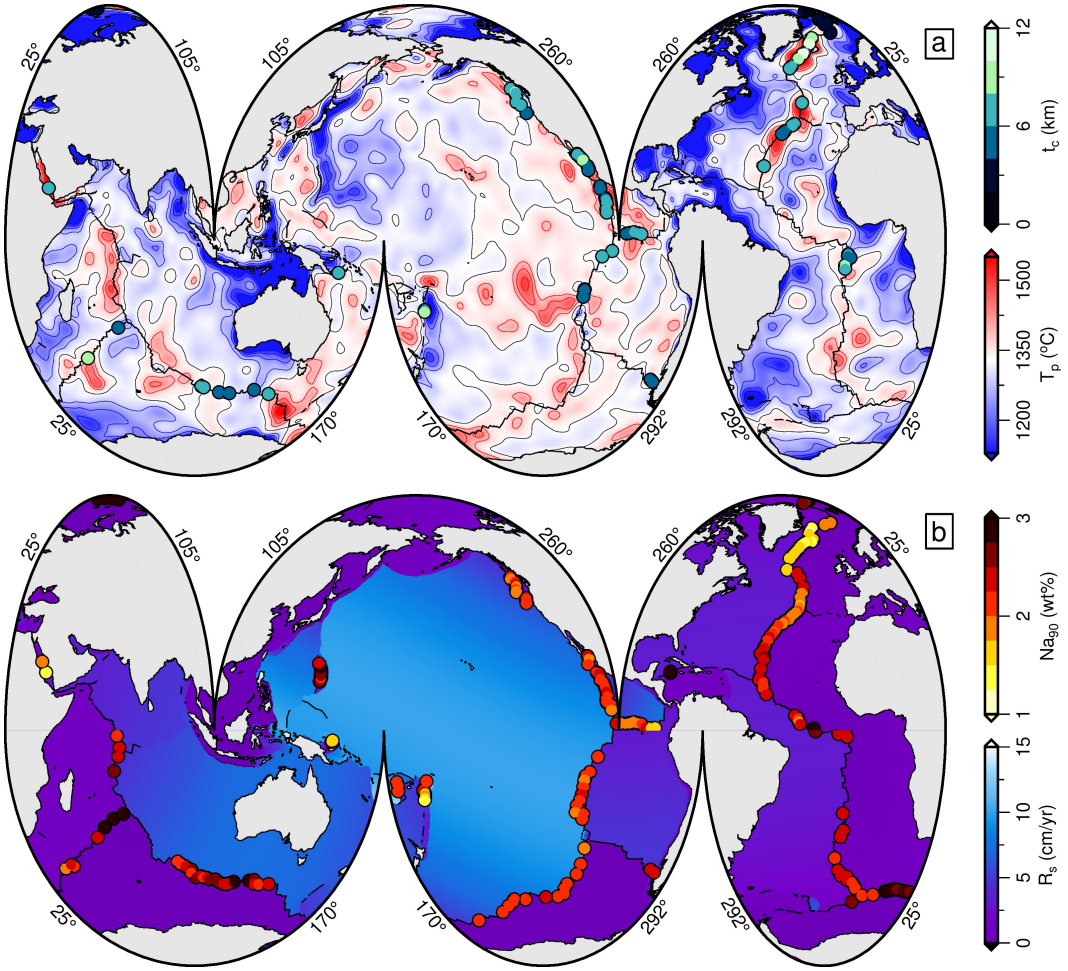

Figure 5. Geographic distribution of mid-oceanic ridge observations. a) Segmented Mollweide projection of globe showing estimate of potential temperature (T_p) at 150 $\pm$ 25 km depth (Richards et al., 2020). Circles = loci of oceanic crustal thickness estimates (Hoggard et al., 2017). b) Grid of present-day plate velocity magnitude (Argus et al., 2011). Circles = loci of mid-oceanic ridge segments with basaltic rock trace element data coloured by average Na_{90} value (Gale et al., 2014).

of low crustal thicknesses at $R_s < 2.1$ cm yr^{-1}, a sharp increase in crustal thicknesses when $R_s \geq 2.1$ cm yr^{-1}, and a subsequent slow decrease in crustal thickness as a function of R_s, is observed, to a certain degree, in our global crustal-thickness database (after filtering to only include ridges overlying ambient mantle i.e., $T_p = 1325 \pm 25$ °C; Figure 6g). However, it is unclear to what extent observed crustal thicknesses decrease at $R_s \geq 2.1$ cm yr^{-1} and at these half-spreading rates simulated crustal thicknesses are ~ 1 km less than observed crustal thicknesses (Figure 6g).

Since the melting region beneath mid-oceanic ridges tapers towards the ridge axis, narrowing the magmatic focusing distance decreases the relative contribution of deep, incompatible-element rich melts (Figure 6d–f). Therefore, our simulations predict a decrease in Na_2O concentrations as spreading rates increase. This predicted decrease is somewhat matched by the distribution of observed Na_{90} values. We find that the highest Na_{90} values decrease as a function of R_s, but that the lowest Na_{90} values remain at ~ 2 wt%

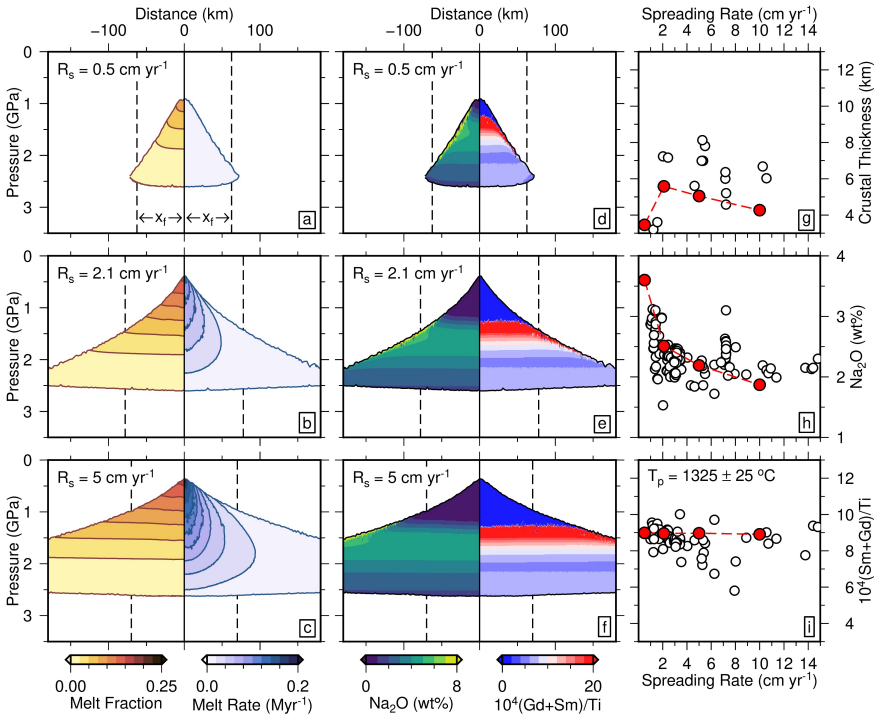

Figure 6. Melt region geometry at mid-oceanic ridges as a function of half-spreading rate (R_s). a) Ridge-centered simulation with left- and right-hand sides coloured by melt fraction and melting rate, respectively. Simulation run with a potential temperature (T_p) of 1325 °C and a R_s of 0.5 cm yr^{-1}. b–c) Same as panel a but with different R_s as indicated in top left corner of each panel. d) Same as panel a but left- and right-hand sides coloured by Na_2O concentration and 10^4(Sm+Gd)/Ti within the instantaneous melt phase, respectively. e–f) Same as panel d but with different R_s as indicated in top left corner of each panel. g) Crustal thickness as function of R_s. Red circles and dashed lines = calculated crustal thicknesses within melt focusing region from cases shown in panels a–c and Supplementary Figure 7g; white circles = observed crustal thicknesses at mid-oceanic ridge segments with $T_p = 1325 \pm 25$ °C (Gale et al., 2013; Hoggard et al., 2017; Richards et al., 2020). h) Same as panel g with predicted Na_2O concentrations compared to Na_{90} values at each ridge segment (Gale et al., 2013, 2014; Richards et al., 2020). i) Same as panel g with predictions compared to average 10^4(Sm+Gd)/Ti values at each ridge calculated using samples with MgO > 8.5 wt%.

at all spreading rates (Figure 6h; Gale et al., 2013). Varying spreading rate or x_f does not significantly affect 10^4(Gd+Sm)/Ti values since, in all cases, melting is sufficiently extensive that this ratio remains close to to that of the original mantle source (Figure 6i).

4.3 Effect of Mantle Composition and Mineralogy on Melting

Mantle composition and mineralogy exert a strong influence on both melt productivity and composition (Section 3). Fertile mantle has greater concentrations of incompatible elements and volatiles, and a greater abundance of clinopyroxene than depleted mantle (Gast, 1968; Morgan, 1968; Walter, 1998). Consequently, if T_p and R_s are held constant, the melting region beneath a ridge underlain by more fertile mantle will be deeper,

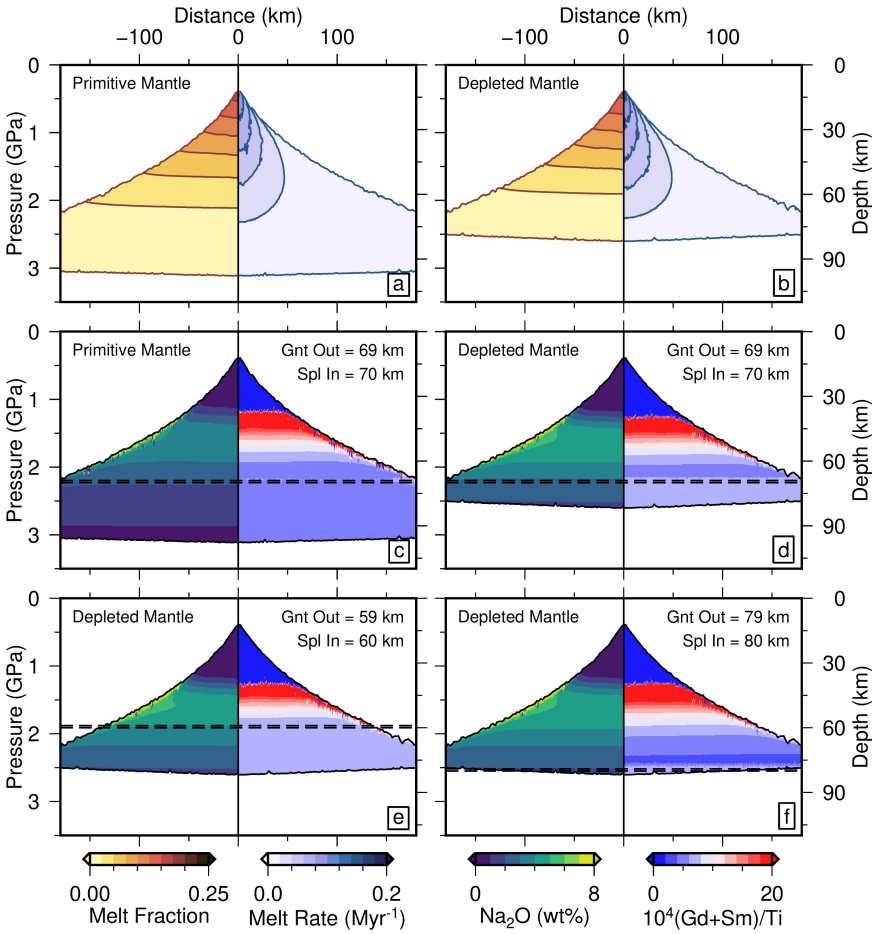

Figure 7. Melt region geometry at mid-oceanic ridges as a function of mantle mineralogy and composition. a) Ridge-centered simulation with left- and right-hand sides coloured by melt fraction and melting rate, respectively. Simulation run with a potential temperature of 1325 °C and a half-spreading rate of 2.1 cm yr^{-1}. Simulation has primitive mantle composition and the spinel garnet transition zone is between 69–70 km depth. b) Same as panel a but with depleted mantle composition. c/d) Same as panels a/b but left- and right-hand sides coloured by Na_2O concentration and 10^4(Sm+Gd)/Ti within the instantaneous melt phase, respectively. Dashed lines denote spinel-garnet-transition zone depths e–f) Same as panel d but with different spinel-garnet-transition-zone depths as indicated in top right corner of each panel.

since increasing volatile content of the mantle deepens the solidus (Katz et al., 2003). Mid-oceanic ridge crustal thicknesses and basaltic compositions may therefore be more sensitive to mantle source heterogeneity than to temperature or spreading rate (e.g., Niu & O'Hara, 2008; Niu, 2016). Here, we assess the sensitivity of our modelling results to mantle composition.

To ascertain the extent to which source fertility and spinel-garnet-transition-zone depth affect the cumulative melt compositions, we perform simulations where these parameters are varied between extrema (Figure 7). In these cases, T_p and R_s are 1325 °C and 2.1 cm yr^{-1}, respectively. Our primitive source has 180 ppm more H_2O than our depleted source and, so, increasing mantle fertility from depleted to primitive mantle increases the pressure of the solidus from $\sim 2.6 - 3.2$ GPa (Figure 7a,b). The more ex-

tensive melting region of the primitive mantle case generates crustal thicknesses 0.35 km greater than those calculated for the comparable depleted mantle case. Clinopyroxene is more abundant in fertile mantle and, as noted above, Na is more compatible within clinopyroxene-rich mantle. As a result, we calculate lower Na concentrations in the cumulative melts delivered to the ridge axis in the fertile mantle case (2.02 wt% compared to 2.51 wt% for the depleted mantle case; Figure 7c,d). As mantle temperatures increase, we expect that the difference between Na concentrations in fertile and depleted mantle simulations to reduce as clinopyroxene is progressively consumed. At the highest potential temperatures examined, where clinopyroxene is exhausted during melting, we would expect primitive mantle to generate crust with higher Na concentrations than depleted mantle since fertile mantle contains a higher initial concentration of incompatible elements. 10^4(Gd+Sm)/Ti is lower in our primitive mantle source than in our depleted mantle source. As a result, the 10^4(Gd+Sm)/Ti value recorded for our primitive mantle case is lower than for our depleted case (8.08 and 8.96, respectively). However, both values are close to the observed global average along mid-oceanic ridges (8.61 ± 0.47 O'Neill & Jenner, 2016).

At the spinel-garnet-transition zone, garnet and olivine are replaced by a combination of orthopyroxene and spinel. Increasing the spinel-garnet-transition-zone depth does not greatly affect Na_2O concentrations since Na_2O is most sensitive to the amount of clinopyroxene in the mantle, which does not change at this transition (Figure 7e,f). The incompatibility of Ti in the mantle source sharply increases at depths shallower than the spinel-garnet-transition zone. Gd and Sm also become more incompatible in the spinel stability field, but incompatibility slowly increases as pressure decreases, rather than being strongly focussed at the spinel-garnet transition itself, as is the case with Ti (Figure 3). As a result, a deep spinel-garnet-transition zone generates deep melts with low 10^4(Gd+Sm)/Ti ratios (Figure 7f). These melts are down-weighted in the calculation of the average 10^4(Gd+Sm)/Ti ratio at the ridge-axis, since deeper melts have lower melting rates. Consequently, 10^4(Gd+Sm)/Ti decreases from 9.26 to 8.81 as the spinel-garnet-transition-zone depth increases from 59–60 to 79–80 km. Although the elements and ratios investigated here are not greatly affected by spinel-garnet-transition-zone depth, we note that this does have a significant effect on the concentrations of elements that are more compatible in garnet than other upper-mantle minerals (Kay & Gast, 1973).

We note that in our simulations we do not consider the relative densities of fertile and depleted mantle. Fertile mantle is denser than depleted mantle (Jordan, 1978). A mid-oceanic ridge underlain by more fertile mantle may therefore sit deeper beneath the sea surface. Deeper ridges will cease melting at higher pressures than shallow ridges, which may effect the composition of erupted melts (Niu & O'Hara, 2008). However, mantle density and, therefore, ridge depth, may be more sensitive to temperature variations than compositional variations, as highlighted by the negative correlation between sub-solidus mantle shear-wave velocities and ridge depth (Dalton et al., 2014). For a list of all mid-oceanic ridge simulation results see Supplementary Table S3.

5 Application to Lithospheric Steps

In intra-plate magmatic settings adjacent to lithospheric steps, melting is typically deeper, less productive and shorter lived that at mid-oceanic ridges (Duvernay et al., 2021). To ensure that our approach is also valid in these low-melt-productivity environments, we construct and analyse a series of coupled geochemical-geodynamical simulations that are applicable for such intra-plate settings.

Edge-driven convective cells form along steps in lithospheric thickness, for example where thick continental interiors abut thinner continental or oceanic margins (Figure 1b; King & Anderson, 1998). Locations where these cells have been suggested as causal mechanisms for present-day volcanism include eastern Australia, Cameroon and the Col-

orado Plateau (Davies & Rawlinson, 2014; Adams et al., 2015; Ballmer et al., 2015; Afonso et al., 2016; Rawlinson et al., 2017). In these regions, intricate details of 3-D lithospheric architecture, the magnitude and direction of plate motion and/or asthenospheric flow, and potential complications arising from complex flow induced by adjacent subducting slabs and/or mantle plumes can influence the distribution and extent of melting (Ballmer et al., 2007; Conrad et al., 2011; Davies & Rawlinson, 2014; Kennett & Davies, 2020; Duvernay et al., 2021). As such, replicating specific melting observations at one of these locations is beyond the scope of this paper. Instead, our aim is to reproduce expected first-order differences between melting at mid-oceanic ridges and at lithospheric steps, and to confirm that these simulations generate similar melt chemistry to lavas observed adjacent to lithospheric steps. Furthermore, we test the sensitivity of our 2-D lithospheric step simulations to the thickness of the overlying oceanic thermal-boundary-layer, highlighting the role of pressure and the overlying lid in dictating melt compositions.

In the case presented in Figure 8a, we impose an initial oceanic lithospheric thickness (B_L) of 50 km, the spinel-garnet-transition zone is placed at 69–70 km depth, and an equal mix of primitive and depleted mantle with a water content of 200 ppm is assumed. Under these conditions the solidus is situated at ~ 90 km depth and, hence, melt is generated in locations where asthenospheric mantle upwells at depths $\lesssim 90$ km. The temperature contrast between cold continental lithosphere and horizontally adjacent asthenosphere causes the asthenosphere close to the continent to cool. As this asthenosphere cools, its density increases and it begins to sink, displacing deeper asthenosphere which upwells as a passive return flow (see grey arrows in Figure 8b-h). This convection cell intensifies as the instability grows and continuously supplies fresh mantle to the the base of the plate, thus maintaining a melting zone close to the lithospheric step (Figures 8b–e). Over time, the oceanic lithosphere thickens through thermal diffusion. This thickening decreases the distance between the solidus and the base of the thermal boundary layer and, as a result, the melting region becomes increasingly restricted. Consequently, cases with thicker initial thermal boundary layers cease melting sooner and have lower maximum melt fractions (Figure 8e–j). The edge-driven cell next to the lithospheric step continuously supplies hot asthenosphere to the base of the plate and retards the rate of conductive cooling. Nevertheless, by 25 Myr, melting has ceased in all simulations.

Variations in the extent and depth of melting are reflected in the compositions of the melts generated. When calculating erupted-melt compositions from these simulations, we weight melts according to their melting rates and assume that all melt is instantaneously extracted (i.e., A encompasses the whole melting region; Equation 18). La is more incompatible within the mantle than Sm and hence higher melt fractions yield lower La/Sm ratios within the integrated melt (Figure 3). Accordingly, melts generated towards the beginning of each simulation have lower La/Sm ratios (Figure 8k). Yb is much more compatible in garnet than spinel, and so Sm/Yb values are sensitive to the proportion of melting in the spinel and garnet stability fields. As the depth to the top of the melt column increases, melting ceases within the spinel stability field (Figure 8j). As each simulation progresses, Sm/Yb values therefore increase as a higher proportion of melting occurs in the garnet stability field.

The geochemical results from our simulations resemble compositions observed along present-day lithospheric steps. Using a recent global compilation, average La/Sm values for high-MgO basalts from Cameroon, Western USA and the Newer Volcanic Province, Australia, are 5.53 ± 0.77, 5.17 ± 1.09 and 5.94 ± 2.42, respectively (Ball et al., 2021). Both geochemical modeling and mantle temperature estimates derived from seismic tomographic models suggest that the lithosphere beneath these volcanic provinces is ~ 50–65 km thick (Hoggard et al., 2020; Ball et al., 2021). Under these conditions, our simulations predict lower La/Sm values than those recorded at the aforementioned locations (La/Sm ≈ 4; Figure 8k). However, complexities that we do not include, such as the presence of trace-element-enriched fusible mantle phases, crystal fractionation, and the in-

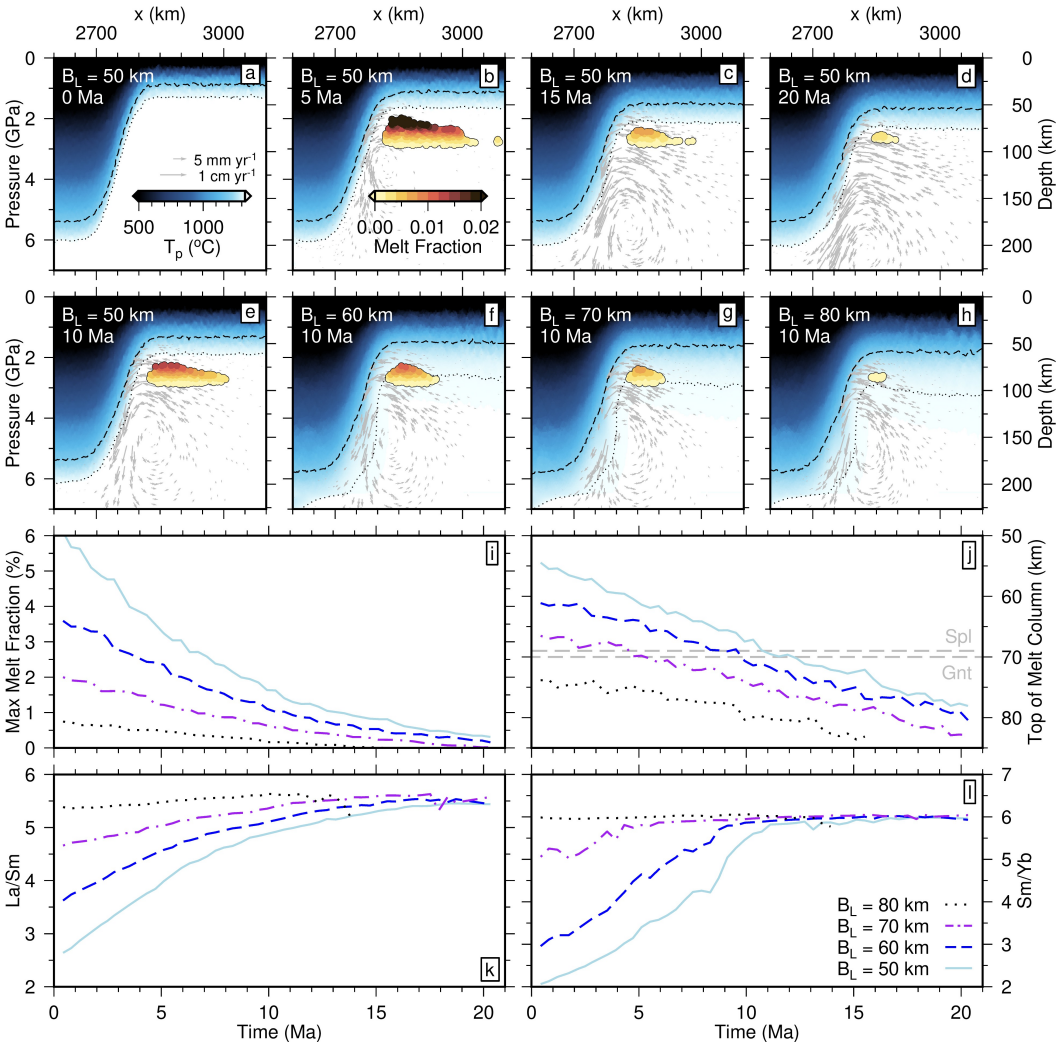

Figure 8. Melting geometry along lithospheric steps as a function of initial thermal-boundary-layer thickness (B_L) and time. a–h) Lithospheric-step centred melting simulation with background coloured by temperature; dotted/dashed contours = isothermal surfaces with temperature of 1325/1200 °C; coloured circles = melt fraction on each particle; B_L and duration the simulation has run for indicated top-left corner. i) Maximum melt fraction as a function of simulation time for four simulations with B_L of 50–80 km. j) Top of melt column as a function of simulation duration; dashed gray lines = top and bottom of spinel-garnet transition zone. k) Cumulative La/Sm ratio in the melt as a function of simulation duration. l) Cumulative Sm/Yb ratio in the melt as a function of simulation duration.

corporation of metasomatised lithosphere can act to increase La/Sm values in the final melt.

Given the strong sensitivity of our modelling predictions to thermo-chemical structure, it is clear that accurate replication of incompatible element concentrations and ratios of lavas at lithospheric steps requires full integration of all available geochemical and geophysical constraints. Such efforts have begun, particularly those exploiting geophysical observations of lithospheric structure and thickness (e.g., Rawlinson et al., 2017).

However, the use of geochemical constraints remains in its infancy and will doubtless become a fruitful avenue for future research. It is therefore not surprising that our predictions do not perfectly match the composition of igneous rocks observed at some of these locations. Nevertheless, the results presented in this study are encouraging. Our findings demonstrate that BDD21 provides a framework within which to test different geodynamical scenarios, and to discount those that cannot be reconciled with geochemical observations from igneous rocks.

6 Discussion

In this study, we have presented BDD21, a new peridotite melting parameterization that predicts melt productivity and chemistry through space and time. We coupled BDD21 to incompressible, single-phase-flow simulations generated using Fluidity, to replicate mantle melting at two contrasting geologic settings: mid-oceanic ridges and lithospheric steps.

Our mid-oceanic-ridge simulations were analysed over a wide range of spreading rates and mantle temperatures. They reproduce key melt-related diagnostics that are consistent with those observed at present-day ridge segments: (i) crustal thickness and incompatible-element concentrations (e.g., Na_2O) increase and decrease as a function of mantle temperature, respectively; (ii) crustal thickness and incompatible-element concentrations are less sensitive to spreading rate than to mantle temperature at plate velocities > 1.5 cm yr^{-1}; and (iii) 10^4(Sm+Gd)/Ti is approximately constant across the parameter space examined, as is observed throughout the mid-oceanic-ridge system (Figures 4 and 6; Klein & Langmuir, 1987; White et al., 1992; O'Neill & Jenner, 2016). To our knowledge, our study is the first to reconcile observed mid-oceanic ridge patterns in Na_2O and 10^4(Sm+Gd)/Ti within the same modelling framework.

Our lithospheric step simulations illustrate that melt productivity and composition are strongly sensitive to the thickness of the overlying lithospheric lid. As these simulations progress, melt volumes decrease, incompatible-element concentrations increase, and the proportion of melting in the garnet stability field increases as the melting region is suppressed by the thickening thermal-boundary layer above. Our mid-oceanic ridge and lithospheric step simulations demonstrate that BDD21 can replicate first-order differences in melt distribution and composition between these different geologic settings. This result implies that BDD21 can be used to investigate the geodynamical mantle processes responsible for the emplacement of igneous provinces, both at the present day and into the geological past.

A number of previous studies have calculated melt compositions at mid-oceanic ridges by coupling geochemical melting parameterizations to mantle flow simulations (e.g., McKenzie & O'Nions, 1991; Langmuir et al., 1992; Plank & Langmuir, 1992; Asimow et al., 2004; Gregg et al., 2009; Behn & Grove, 2015; Brown & Lesher, 2016; Brown et al., 2020; Krein et al., 2020). We next consider the implications of our modeling results at mid-oceanic ridges and lithospheric steps, compare BDD21 to other melting parameterizations, discuss uncertainties that are inherent to parameterizations of this nature, and briefly outline potential future research avenues utilizing our approach.

6.1 Observational Uncertainties at Mid-Oceanic Ridges

We use BDD21 to predict primary magmatic compositions. It is important to remember that when we compare these predictions to observations at mid-oceanic ridges, we are comparing to basaltic glasses that represent the vestigial melts of complex magmatic plumbing systems (O'Hara, 1977). Observed Na_2O concentrations are corrected for fractional crystallisation so that the melt is in equilibrium with the upper mantle (Na_{90}; Gale et al., 2014). However, this correction assumes that fractionation occurs in a closed

system, and that plagioclase begins crystallising when MgO wt% < 8.5. Modeling fractional crystallisation in a magmatic system that replenishes over time, or varying the point at which plagioclase begins crystallising, can significantly affect calculated Na_{90} values (e.g., O'Neill & Jenner, 2012; Till et al., 2012). Although corrected compositions should be treated with caution, it is encouraging that our mid-oceanic ridge simulations replicate the broad trends found in two very different geochemical systems - Na_2O and 10^4(Sm+Gd)/Ti. In future, given that each incompatible element behaves differently during fractional crystallisation, it may be informative to use our predictive primary melt compositions as a starting point to investigate these fractional crystallisation processes.

We compare our simulations to mid-oceanic ridges that have potential temperatures that are estimated to be between 1250–1650 °C using techniques that convert from seismic to physical structure (Richards et al., 2020). The hottest segments in the mid-oceanic ridge system, such as those near Iceland and the Galápagos Islands, are underlain by mantle plumes. All our simulations assume passive upwelling in response to plate spreading. However, near plumes, upwelling is likely to be thermally driven by buoyancy contrasts between the hot plume and the surrounding mantle (e.g., Ito & Mahoney, 2005). If upwelling speeds beneath the ridge are increased by an order of magnitude, crustal thicknesses are predicted to increase by a factor of $\sim$ 4–5 and incompatible-element concentrations are also predicted to increase (Maclennan et al., 2001). These aspects are not captured by our simulations. Moreover, we do not account for possible compositional differences between these plumes and depleted mantle (Fitton et al., 1997; T. Jones et al., 2016). A more enriched mantle plume source may be responsible for the slight increase in observed Na_{90} concentrations at temperatures $\gtrsim 1425$ °C (Figure 4h). Moreover, an increase in enriched mantle material may explain observed low 10^4(Sm+Gd)/Ti values (i.e., < 8) at some ridges with $T_p \gtrsim 1500$ °C (Figure 4i). Taken together, these observations suggest that incorporating enriched mantle plumes in future simulations may reduce discrepancies between predicted and observed compositions at higher potential temperatures.

6.2 Mid-Oceanic Ridge Simulation Uncertainties

A significant source of uncertainty within our single-phase flow modeling approach is that we must assume a melt-focusing region (i.e., the region beneath the ridge from which melt is extracted) and/or a melt-extraction efficiency (i.e., the proportion of melt that is extracted at the ridge axis). In Sections 4.1 and 4.2, we assume that the lateral melt-focusing distance (x_f) coincides with the intersection between the anhydrous solidus and $v_z = R_s/3$, and that within the melt-focusing region extraction efficiency is 100% (red circles in Figure 9a,e; Keller et al., 2017). An alternative approach would be to choose values of x_f that best fit crustal thickness observations (blue circles in Figure 9a,e). Here, we investigate the effect of varying x_f on melt diagnostics.

The simulations shown in Section 4.1 yield crustal thickness estimates that exceed those observed, and the difference between calculated and observed crustal thicknesses increases as a function of T_p (Figure 9b). To fit crustal thickness observations, x_f must be reduced to $\sim$ 30 km for simulations with $T_p > 1275$ °C. However, narrowing the melt-focusing region in this way reduces the relative contribution of deeper melts and decreases calculated Na_2O concentrations such that they no longer lie within the observed range (Figure 9c). Calculated 10^4(Sm+Gd)/Ti values are largely unaffected by changing x_f (Figure 9d).

The increasing disparity between predicted and observed crustal thicknesses as potential temperatures increase may instead result from our assumption that all material within the melting region is fusible. The presence of refractory material (i.e., mantle material that does not melt) will reduce calculated crustal thicknesses. If the proportion of fusible material is set to a value $< 100\%$, crustal thickness reduces as a function of

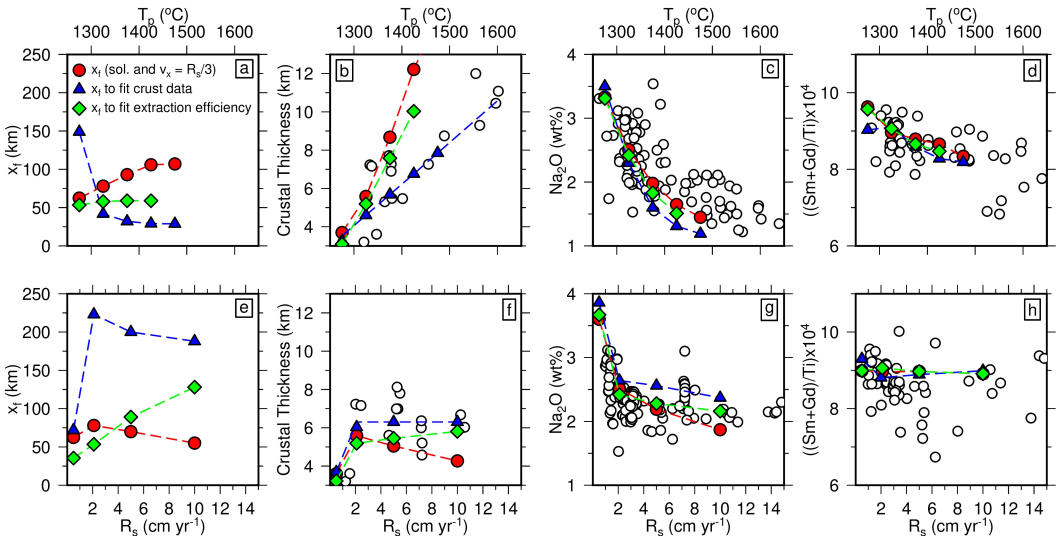

Figure 9. Varying x_f to fit mid-oceanic ridge crustal thickness observations. a) x_f as a function of T_p. Red circles = x_f values determined using intersection of anhydrous solidus and $v_z = R_s/3$. Blue triangles = x_f required to generate average observed crustal thickness. Green diamonds = x_f required to fit extraction efficiency data from Keller et al. (2017). b) Crustal thickness as a function of T_p. Colored symbols and dashed lines = calculated crustal thicknesses within melt focusing regions defined in panel a; white circles = observed crustal thicknesses at mid-oceanic ridge segments with $R_s = 2.1 \pm 1$ cm yr^{-1} (Gale et al., 2013; Hoggard et al., 2017; Richards et al., 2020). c) Same as panel b with predicted Na_2O concentrations compared to Na_{90} values at each ridge segment (Gale et al., 2013, 2014; Richards et al., 2020). d) Same as panel b with simulation outputs compared to average 10^4(Sm+Gd)/Ti values at each ridge calculated using samples with MgO > 8.5 wt%. e–h) Same as panels a–d but showing melt diagnostics as function of R_s. Global databases filtered to include ridges above mantle with $T_p = 1325 \pm 25$ °C.

the absolute reduction in melt volume (e.g., Keller et al., 2017). An analogous case can be made for decreasing crustal thickness by reducing extraction efficiency within the melt-focusing region. We note that varying the concentration of refractory material within the melt region or the melt-extraction efficiency will change calculated crustal thicknesses without affecting melt composition, unless the amount of refractory material in the source and/or extraction efficiency varies in space.

Away from slow spreading centers and mantle plumes, oceanic crustal thicknesses show little variation (6.3±0.8 km; White et al., 2001). Like many previous studies, our simulations suggest that this range of crustal thicknesses can be generated by ambient mantle potential temperatures of ∼ 1350 °C (e.g., Langmuir et al., 1992; Bown & White, 1994; Brown et al., 2020). To maintain a crustal thickness of 6.3 km within our simulations at a constant T_p of 1325 °C and at a range of spreading rates requires x_f to increase by ∼ 150 km (Figure 9e,f). Such a substantial widening of the melt-focusing region arises due to the sharp reduction of melt productivity in distal regions (i.e., smaller melt volume contributions far from the ridge axis), and it leads to a rise of calculated Na_2O concentrations (Figure 9g). However, such an increase in x_f is likely unrealistic. Instead, raising the ambient potential temperature in our simulations from 1325 °C to ∼ 1350 °C would increase and decrease calculated crustal thicknesses and Na_2O con-

centrations, respectively, and, thus, improve our fit to observational data without requiring any widening of the melt-focusing region.

In Section 4.2, we predict that crustal thicknesses decrease as a function of spreading rate. To obtain these values, we make use of the observation of Keller et al. (2017) that the x_f can be approximated through a relationship between upwelling rate, spreading rate and depth of the anhydrous solidus. Thereby, our predicted decrease occurs because, using the approximation of Keller et al. (2017), x_f in our simulations narrows as R_s increases (when $R_s > 2.1$ cm yr^{-1}; Figure 9e). However, within the Keller et al. (2017) simulations, x_f increases as a function of R_s and calculated crustal thicknesses remain approximately constant. Such a change in behavior likely results from differences between the thermal and rheological structure of our simulations and those of Keller et al. (2017). Alternatively, we can define x_f according to the extraction efficiency observed in the simulations of Keller et al. (2017). In this approach, the total volume of melt generated within a distance x_f from the ridge axis is equal to the extraction efficiency of the whole melting region (green line in Figure 9; see Supplementary Materials for method description). This method yields increasing values of x_f as a function of R_s, in agreement with Keller et al. (2017) (Figure 9e). Redefining x_f to fit extraction efficiency yields in a better fit to crustal thickness data and little change to calculated geochemical diagnostics. In future, documenting trade-offs between crustal thickness, mantle composition, melt focusing, extraction efficiency, T_p, and R_s on the outputs of our coupled geochemical-geodynamical simulations may play an important role in refining our understanding of mid-oceanic ridge systems.

6.3 Lithospheric Step Simulation Uncertainties

The uncertainties that exist when predicting melt compositions at mid-oceanic ridges (e.g., lithospheric processing, melt focusing and source heterogeneity) are amplified at intraplate settings, since melt fractions are lower and the thermo-chemical structure and underlying flow-regime are less well constrained. However, igneous rock compositions represent one of the few viable constraints for investigating how the upper mantle's thermo-chemical structure changes through space and time, and accordingly, the results generated by BDD21 deserve careful consideration. Our edge-driven convection simulations show that, over time, the thermal-boundary layer at lithospheric steps should cool and thicken. This thickening restricts the melting region and generates melts that are increasingly enriched in incompatible elements and with more-pronounced garnet signatures (e.g., high Sm/Yb; Figure 8). This pattern is a robust prediction of our models and, as such, may be observed in locations where edge-driven convection has been postulated as the driving mechanism of volcanism. Future work should therefore analyse the spatio-temporal evolution of lavas at volcanic provinces adjacent to lithospheric steps to determine whether or not this trend is observed.

6.4 Comparison to Other Mantle Melting Parameterizations

Our approach initialises the upper mantle as homogeneous peridotite. However, multiple lithologies, including harzburgitic and pyroxenitic variants, exist within the mantle (e.g., Allègre & Turcotte, 1986; Stracke, 2012). Each lithology has a different mineralogy, solidus, and composition and, accordingly, the distribution and composition of melts will depend strongly on the upper mantle's lithological make-up. Most modern geochemical parameterizations, like BDD21, make use of melting experiments conducted on MM3 and KR4003 lherzolites to constrain melt stoichiometry (Baker & Stolper, 1994; Walter, 1998; Falloon et al., 1999). However, some parameterizations incorporate additional constraints to broaden their applicability to different compositions. Two such parameterizations, REEBOX PRO and Petrogen, have been used to study melt chemistry at mid-oceanic ridges (Brown & Lesher, 2016; Krein et al., 2020).

REEBOX PRO uses the thermodynamic solver Perple X to parameterize melt stoichiometry as a function of P and X for depleted peridotite, harzburgitic and pyroxenitic lithologies (Connolly, 2005; Brown & Lesher, 2016). Using a purely peridotitic parameterization such as BDD21 to predict melt compositions in a region that contains pyroxenite or harzburgite could under- or over-predict melt productivity (Katz et al., 2003; Lambart et al., 2016). Pyroxenites can vary greatly in composition and melts will react with each wall-rock lithology differently on their way to the surface (e.g., Yaxley & Green, 1998; Lambart et al., 2012; Katz & Weatherley, 2012). Furthermore, the distribution of lithologies with different densities within the upper-mantle will affect how mantle flow and, therefore, melt geometry, develops through time (e.g., Ito & Mahoney, 2005). Although Bayesian inversion schemes can be used to constrain the lithological make-up of a heterogeneous mantle beneath a mid-oceanic ridge using a simple melt geometry and a perfectly mixed mantle (Brown et al., 2020), it is currently computationally intractable to implement such a scheme in combination with a geodynamical simulation.

Rather than relying on a thermodynamic solver, Petrogen includes a wider variety of peridotite melting experiments to constrain modal mineralogy (Krein et al., 2020). Since the peridotites used in these experiments have different compositions, the calculated solidus and melt stoichiometry are also functions of major element chemistry (Till et al., 2012). This framework allows both the major and trace element compositions of melts to be calculated, and for melts to re-equilibrate with their surroundings during ascent (Krein et al., 2020). Petrogen reproduces the mineral modes from the majority of peridotite melting experiments, including those used to constrain BDD21 (e.g., Walter, 1998). However, the agreement between observed and calculated clinopyroxene proportions for some starting compositions is poor (correlation coefficient = 0.4–0.45; Krein et al., 2020). Since many incompatible elements, including Na, La, Sm and Gd, are most compatible in clinopyroxene, the concentrations of these elements are particularly sensitive to the proportion of clinopyroxene in the mantle source. Therefore, trace element concentrations calculated using some peridotite compositions should be treated with caution. Nevertheless, the incorporation of major elements means that Petrogen offers functionality that cannot currently be replicated in BDD21 or REEBOX PRO. Both REEBOX PRO and Petrogen predominantly rely on fixed partition coefficients (Brown & Lesher, 2016; Krein et al., 2020). Using the parameterization of Blundy et al. (1995), the partition coefficient for Na in clinopyroxene varies from 7.45 at the solidus to 0.15 beneath the ridge axis in our mid-oceanic ridge simulation (where $R_s = 2.1$ cmyr^{-1} and $T_p = 1325$ °C). We believe that including pressure, temperature and composition dependent partition coefficients can significantly affect predicted element concentrations, and so their inclusion in BDD21 can be considered an improvement on existing parameterizations.

The applicability of each melting parameterization to other geologic settings and to geodynamical simulations is defined by its geochemical framework. REEBOX PRO calculates melt composition at mid-oceanic ridges using the "residual mantle column" method pioneered by Langmuir et al. (1992) and Plank and Langmuir (1992). This method assumes that when a mid-oceanic ridge is in steady state, flow is horizontal away from spreading centres so that the distribution of melt depletion within a column of mantle outside of the melt region can be used to calculate the composition of the crust above it (Langmuir et al., 1992). This elegant solution removes the necessity to accurately constrain the geometry of the melting region and can be augmented with additional complexity such as mantle temperature variations and buoyancy-driven flow (e.g., Plank & Langmuir, 1992; Brown & Lesher, 2014). However, using this framework limits REEBOX PRO to calculating melting at spreading centers and it cannot be used to test how physical parameters, such as including a temperature and strain-rate dependent viscosity, impact melt composition. In contrast, Petrogen can be used to calculate melt compositions based on outputs from geodynamical simulations (Krein et al., 2020). One key advantage of the Petrogen approach is that, unlike the other schemes that rely on the melting parameterization of Katz et al. (2003), the solidus in Petrogen is compositionally dependent. How-

ever, since the solidus is calculated in the posterior within the geochemical calculation, temperature and viscosity variations associated with melting are not fed back into the geodynamical simulation (Behn & Grove, 2015). Moreover, the polybaric melting functions used in Petrogen are simplistic compared to those used by REEBOX PRO and BDD21 ($\frac{dF}{dP}$ is currently either set as a constant, e.g., 10% GPa^{-1}, or set to linearly increase between the solidus and the surface; Krein et al., 2020). At present, BDD21 can only estimate trace element compositions of melts generated within a homogeneous peridotite mantle, and so it does not currently offer the geochemical flexibility of parameterizations like REEBOX PRO and Petrogen. However, unlike these parameterizations, BDD21 links seamlessly to a geodynamical modelling framework on the fly, to calculate melting through space and time. As such, it provides an opportunity to understand the how melting and melt composition evolve in different geologic settings, and in response to changing mantle conditions.

7 Conclusions and Future Directions

We have presented BDD21, a new geochemical melting parameterization for calculating melt incompatible element concentrations as a function of temperature, pressure, melt fraction and mantle composition. This parameterization is designed in such a way that it can be seamlessly coupled with geodynamical simulations, as demonstrated herein through the Fluidity computational modelling framework. The versatility of our combined geochemical-geodynamical approach is demonstrated in the context of melting at two geologic settings: mid-oceanic ridges and lithospheric steps. Our simulations reproduce first-order differences in melt volumes and compositions between these settings. Furthermore, we replicate geological and geochemical observations throughout the present-day mid-oceanic ridge system. Taken together, our results imply that coupled geochemical-geodynamical approaches, such as the one advocated herein, will reveal new insights into the mechanisms and processes controlling magmatism, both at the present day and into the geological past.

For simplicity, we have only analysed results for a handful of incompatible elements (e.g., Na, Ti, La, Sm, Gd and Yb). However, BDD21 can currently calculate melt concentrations for 34 elements, and calculating additional element concentrations incurs limited computational cost. Furthermore, the modular nature of BDD21 allows for seamless refinement of the current framework as more experimental data become available, as well as future incorporation of heterogeneous mantle lithologies and major-element systematics. These potential improvements would increase the versatility of BDD21 but also highlight the number of unknowns present when conducting studies of this nature. We believe that analysing how melt chemistry evolves through space and time in response to varying individual parameters in isolation, such as mantle T_p, lithospheric geometry and thickness, source lithology, mantle rheology, plate velocity, or the presence/absence of mantle plumes, will be a fruitful avenue for improving our understanding of past and present magmatic phenomena.

8 Data and Software Availability Statement

The BDD21 melting parameterization can be accessed via `https://github.com/Patol75/BDD21`. The Fluidity computational modeling framework, including source code, demonstrable examples and documentation, are available from `https://fluidityproject.github.io/`; the latest release, with tag 4.1.18 and which we used for the simulations presented herein, is archived at `https://doi.org/10.5281/zenodo.4896641`.

Appendix A Physical Parameters of Geodynamical Simulations

Table A1. Physical parameters used in the mid-oceanic ridge simulations examined herein. UD = user-defined variable.

Quantity	**Symbol**	**Units**	**Value**
Gravity	g	m s^{-2}	9.81
Coefficient of thermal expansion	α	K^{-1}	3×10^{-5}
Thermal diffusivity	κ	m^2 s^{-1}	10^{-6}
Reference density	ρ_s	kg m^{-3}	3300
Surface temperature	T_s	K	273
Mantle temperature	T_m	K	UD
Gas constant	R	J K^{-1} mol^{-1}	8.3145
Max. viscosity	$\mu_{\max}$	Pa s	10^{25}
Min. viscosity	$\mu_{\min}$	Pa s	10^{18}
Half spreading rate	R_s	cm yr^{-1}	UD
Diffusion creep			
Activation energy	E	kJ mol^{-1}	300
Activation volume	V	cm^3 mol^{-1}	4
Prefactor	A	Pa^{-n} s^{-n}	3×10^{-11}
Exponent	n	-	1
Dislocation creep			
Activation energy	E	kJ mol^{-1}	540
Activation volume	V	cm^3 mol^{-1}	16
Prefactor	A	Pa^{-n} s^{-n}	5×10^{-16}
Exponent	n	-	3.5

Table A2. Physical parameters used in the EDC simulations examined herein. UD = user-defined variable.

Quantity	**Symbol**	**Units**	**Value**
Gravity	g	m s^{-2}	9.8
Coefficient of thermal expansion	α	K^{-1}	3×10^{-5}
Thermal diffusivity	κ	m^2 s^{-1}	6×10^{-7}
Mantle density		kg m^{-3}	3370
Continental density		kg m^{-3}	3300
Crust density		kg m^{-3}	2900
Surface temperature	T_s	K	290
Mantle temperature	T_m	K	1598
Adiabatic gradient		$K.km^{-1}$	0.4
Oceanic lithosphere age		Myr	UD
Continent depth		km	200
Step width		km	200
Gas constant	R	J K^{-1} mol^{-1}	8.3145
Activation energy	E	kJ mol^{-1}	350
Activation volume	V	cm^3 mol^{-1}	6.8
Prefactor	A	Pa^{-1}	8.6×10^{-8}
Max. viscosity	$\mu_{\max}$	Pa s	10^{24}
Min. viscosity	$\mu_{\min}$	Pa s	10^{18}
Water Content (Melting)		ppm	200

Acknowledgments

P.B. acknowledges support by Geoscience Australia's Exploring for the Future Program and National Science Foundation Award number EAR-5329212. T.D. is funded by an ANU PhD Scholarship (International) Full-Time (737/2018). D.R.D. acknowledges support from the Australian Research Council (ARC), under DP170100058 and the Australian Research Data Commons (ARDC) and AuScope, both of which are funded by NCRIS. Numerical simulations were undertaken on the NCI National Facility in Canberra, Australia, which is supported by the Australian Commonwealth Government. We are grateful to K. Czarnota, S. Ghelichkhan, M. Klöcking, S. C. Kramer, A. Gibson, C. Mathews, F. M^{c}Nab, H. O'Neill and C. Wilson for advice at various stage of this research. Figures were prepared using Generic Mappin Tools software (Wessel et al., 2013).

References

Adams, A. N., Wiens, D. A., Nyblade, A. A., Euler, G. G., Shore, P. J., & Tibi, R. (2015). Lithospheric instability and the source of the Cameroon Volcanic Line: Evidence from Rayleigh wave phase velocity tomography. *Journal of Geophysical Research: Solid Earth*, *120*(3), 1708–1727.

Afonso, J. C., Rawlinson, N., Yang, Y., Schutt, D. L., Jones, A. G., Fullea, J., & Griffin, W. L. (2016). 3-d multiobservable probabilistic inversion for the compositional and thermal structure of the lithosphere and upper mantle: Iii. thermochemical tomography in the western-central us. *Journal of Geophysical Research: Solid Earth*, *121*(10), 7337–7370.

Allègre, C. J., & Turcotte, D. L. (1986). Implications of a two-component marble-cake mantle. *Nature*, *323*(6084), 123–127.

Argus, D. F., Gordon, R. G., & DeMets, C. (2011). Geologically current motion of 56 plates relative to the no-net-rotation reference frame. *Geochemistry, Geophysics, Geosystems*, *12*(11).

Asimow, P. D., Dixon, J. E., & Langmuir, C. H. (2004). A hydrous melting and fractionation model for mid-ocean ridge basalts: Application to the Mid-Atlantic Ridge near the Azores. *Geochemistry, Geophysics, Geosystems*, *5*(1).

Asimow, P. D., & Langmuir, C. H. (2003). The importance of water to oceanic mantle melting regimes. *Nature*, *421*(6925), 815–820.

Baker, M. B., & Stolper, E. M. (1994). Determining the composition of high-pressure mantle melts using diamond aggregates. *Geochimica et Cosmochimica Acta*, *58*(13), 2811–2827.

Ball, P. W., White, N. J., Maclennan, J., & Stevenson, S. N. (2021). Global influence of mantle temperature and plate thickness on intraplate volcanism. *Nature Communications*, *12*(2045), 1–13.

Ballmer, M. D., Conrad, C. P., Smith, E. I., & Johnsen, R. (2015). Intraplate volcanism at the edges of the Colorado Plateau sustained by a combination of triggered edge-driven convection and shear-driven upwelling. *Geochemistry, Geophysics, Geosystems*, *16*(2), 366–379.

Ballmer, M. D., Van Hunen, J., Ito, G., Tackley, P. J., & Bianco, T. A. (2007). Non-hotspot volcano chains originating from small-scale sublithospheric convection. *Geophysical Research Letters*, *34*(23).

Barry, T., Davies, J., Wolstencroft, M., Millar, I., Zhao, Z., Jian, P., ... Price, M. (2017). Whole-mantle convection with tectonic plates preserves long-term global patterns of upper mantle geochemistry. *Scientific reports*, *7*(1), 1–9.

Becker, T. W., Chevrot, S., Schulte-Pelkum, V., & Blackman, D. K. (2006). Statistical properties of seismic anisotropy predicted by upper mantle geodynamic models. *Journal of Geophysical Research: Solid Earth*, *111*(B8).

Behn, M. D., & Grove, T. L. (2015). Melting systematics in mid-ocean ridge basalts: Application of a plagioclase-spinel melting model to global variations in major element chemistry and crustal thickness. *Journal of Geophysical Research:*

Solid Earth, *120*(7), 4863–4886.

Bercovici, D., Schubert, G., & Glatzmaier, G. A. (1989). Three-dimensional spherical models of convection in the Earth's mantle. *Science*, *244*(4907), 950–955.

Blundy, J., Falloon, T., Wood, B., & Dalton, J. (1995). Sodium partitioning between clinopyroxene and silicate melts. *Journal of Geophysical Research: Solid Earth*, *100*(B8), 15501–15515.

Blundy, J., & Wood, B. (2003). Partitioning of trace elements between crystals and melts. *Earth and Planetary Science Letters*, *210*(3-4), 383–397.

Borghini, G., Fumagalli, P., & Rampone, E. (2010). The stability of plagioclase in the upper mantle: subsolidus experiments on fertile and depleted lherzolite. *Journal of Petrology*, *51*(1-2), 229–254.

Bown, J. W., & White, R. S. (1994). Variation with spreading rate of oceanic crustal thickness and geochemistry. *Earth and Planetary Science Letters*, *121*(3-4), 435–449.

Brice, J. (1975). Some thermodynamic aspects of the growth of strained crystals. *Journal of Crystal Growth*, *28*(2), 249–253.

Brown, E. L., & Lesher, C. E. (2014). North Atlantic magmatism controlled by temperature, mantle composition and buoyancy. *Nature Geoscience*, *7*(11), 820–824.

Brown, E. L., & Lesher, C. E. (2016). Reebox pro: A forward model simulating melting of thermally and lithologically variable upwelling mantle. *Geochemistry, Geophysics, Geosystems*, *17*(10), 3929–3968.

Brown, E. L., Petersen, K. D., & Lesher, C. E. (2020). Markov chain Monte Carlo inversion of mantle temperature and source composition, with application to Reykjanes Peninsula, Iceland. *Earth and Planetary Science Letters*, *532*, 116007.

Connolly, J. A. (2005). Computation of phase equilibria by linear programming: a tool for geodynamic modeling and its application to subduction zone decarbonation. *Earth and Planetary Science Letters*, *236*(1-2), 524–541.

Conrad, C. P., Bianco, T. A., Smith, E. I., & Wessel, P. (2011). Patterns of intraplate volcanism controlled by asthenospheric shear. *Nature Geoscience*, *4*(5), 317–321.

Cooper, C., Farrington, R., & Miller, M. (2021). On the destructive tendencies of cratons. *Geology*, *49*(2), 195–200.

Crisp, J. A. (1984). Rates of magma emplacement and volcanic output. *Journal of Volcanology and Geothermal Research*, *20*(3-4), 177–211.

Dalton, C. A., Langmuir, C. H., & Gale, A. (2014). Geophysical and geochemical evidence for deep temperature variations beneath mid-ocean ridges. *Science*, *344*(6179), 80–83. doi: 10.1126/science.1249466

Davies, D. R., & Rawlinson, N. (2014). On the origin of recent intraplate volcanism in Australia. *Geology*, *42*(12), 1031–1034.

Davies, D. R., Valentine, A. P., Kramer, S. C., Rawlinson, N., Hoggard, M. J., Eakin, C. M., & Wilson, C. R. (2019). Earth's multi-scale topographic response to global mantle flow. *Nature Geoscience*, *12*(10), 845–856.

Davies, D. R., Wilson, C. R., & Kramer, S. C. (2011). Fluidity: A fully unstructured anisotropic adaptive mesh computational modeling framework for geodynamics. *Geochemistry, Geophysics, Geosystems*, *12*(6).

DeMets, C., Gordon, R. G., Argus, D. F., & Stein, S. (1994). Effect of recent revisions to the geomagnetic reversal time scale on estimates of current plate motions. *Geophysical research letters*, *21*(20), 2191–2194.

Duvernay, T., Davies, D. R., Mathews, C., Gibson, A. H., & Kramer, S. C. (2021). Linking lithospheric structure, mantle flow and intra-plate volcanism. *Geochemistry, Geophysics, Geosystems*, *8*(8), 31.

Falloon, T. J., Green, D. H., Danyushevsky, L. V., & Faul, U. H. (1999). Peridotite melting at 1.0 and 1.5 GPa: an experimental evaluation of techniques using

diamond aggregates and mineral mixes for determination of near-solidus melts. *Journal of Petrology*, *40*(9), 1343–1375.

Fitton, J., Saunders, A., Norry, M., Hardarson, B., & Taylor, R. (1997). Thermal and chemical structure of the Iceland plume. *Earth and Planetary Science Letters*, *153*(3-4), 197–208.

Forsyth, D. W. (1993). Crustal thickness and the average depth and degree of melting in fractional melting models of passive flow beneath mid-ocean ridges. *Journal of Geophysical Research: Solid Earth*, *98*(B9), 16073–16079.

Forsyth, D. W., Webb, S. C., Dorman, L. M., & Shen, Y. (1998). Phase velocities of Rayleigh waves in the MELT experiment on the East Pacific Rise. *Science*, *280*(5367), 1235–1238.

Forte, A. M., Quéré, S., Moucha, R., Simmons, N. A., Grand, S. P., Mitrovica, J. X., & Rowley, D. B. (2010). Joint seismic-geodynamic-mineral physical modelling of African geodynamics: A reconciliation of deep-mantle convection with surface geophysical constraints. *Earth and Planetary Science Letters*, *295*(3-4), 329–341.

Frey, F. A., Bryan, W. B., & Thompson, G. (1974). Atlantic Ocean floor: Geochemistry and petrology of basalts from Legs 2 and 3 of the Deep-Sea Drilling Project. *Journal of Geophysical Research*, *79*(35), 5507–5527.

Gale, A., Dalton, C. A., Langmuir, C. H., Su, Y., & Schilling, J.-G. (2013). The mean composition of ocean ridge basalts. *Geochemistry, Geophysics, Geosystems*, *14*(3), 489–518.

Gale, A., Langmuir, C. H., & Dalton, C. A. (2014). The global systematics of ocean ridge basalts and their origin. *Journal of Petrology*, *55*(6), 1051–1082.

Garel, F., Goes, S., Davies, D., Davies, J. H., Kramer, S. C., & Wilson, C. R. (2014). Interaction of subducted slabs with the mantle transition-zone: A regime diagram from 2-D thermo-mechanical models with a mobile trench and an overriding plate. *Geochemistry, Geophysics, Geosystems*, *15*(5), 1739–1765.

Gast, P. W. (1968). Trace element fractionation and the origin of tholeiitic and alkaline magma types. *Geochimica et Cosmochimica Acta*, *32*(10), 1057–1086.

Ghelichkhan, S., Peter, H.-P., & Oeser, J. (2021). Global mantle flow retrodictions for the early Cenozoic using anadjoint method: evolving dynamic topographies, deep mantlestructures, flow trajectories and sublithospheric stresses. *Geophysical Journal International*, *226*(2), 1432–1460.

Ghiorso, M. S., Hirschmann, M. M., Reiners, P. W., & Kress, V. C. I. (2002). The pMELTS: A revision of MELTS for improved calculation of phase relations and major element partitioning related to partial melting of the mantle to 3 GPa. *Geochemistry, Geophysics, Geosystems*, *3*(5), 1–35. doi: 10.1029/2001GC000217

Green, E. C. R., Holland, T. J. B., Powell, R., & White, R. W. (2012). Garnet and spinel lherzolite assemblages in MgO-Al_2O_3-SiO_2 and CaO-MgO-Al_2O_3-SiO_2: Thermodynamic models and an experimental conflict. *Journal of Metamorphic Geology*, *30*(6), 561–577.

Gregg, P., Behn, M., Lin, J., & Grove, T. (2009). Melt generation, crystallization, and extraction beneath segmented oceanic transform faults. *Journal of Geophysical Research: Solid Earth*, *114*(B11).

Hazen, R. M., & Finger, L. W. (1979). Bulk modulus—volume relationship for cation-anion polyhedra. *Journal of Geophysical Research: Solid Earth*, *84*(B12), 6723–6728.

Hill, E., Blundy, J. D., & Wood, B. J. (2011). Clinopyroxene–melt trace element partitioning and the development of a predictive model for HFSE and Sc. *Contributions to Mineralogy and Petrology*, *161*(3), 423–438.

Hindmarsh, A. C. (1983). ODEPACK, a systematized collection of ODE solvers. *Scientific computing*, 55–64.

Hirth, G., & Kohlstedt, D. (2003). Rheology of the upper mantle and the man-

tle wedge: A view from the experimentalists. *Geophysical Monograph-American Geophysical Union*, *138*, 83–106.

Hoggard, M. J., Czarnota, K., Richards, F. D., Huston, D. L., Jaques, A. L., & Ghelichkhan, S. (2020). Global distribution of sediment-hosted metals controlled by craton edge stability. *Nature Geoscience*, *13*(7), 504–510.

Hoggard, M. J., Winterbourne, J., Czarnota, K., & White, N. (2017). Oceanic residual depth measurements, the plate cooling model and global dynamic topography. *Journal of Geophysical Research: Solid Earth*, *122*(3), 2328–2372. doi: 10.1002/2016JB013457

Holland, T. J., Green, E. C., & Powell, R. (2018). Melting of peridotites through to granites: a simple thermodynamic model in the system KNCFMASHTOCr. *Journal of Petrology*, *59*(5), 881–900.

Houseman, G. A., McKenzie, D. P., & Molnar, P. (1981). Convective instability of a thickened boundary layer and its relevance for the thermal evolution of continental convergent belts. *Journal of Geophysical Research: Solid Earth*, *86*(B7), 6115–6132.

Ito, G., & Mahoney, J. J. (2005). Flow and melting of a heterogeneous mantle: 1. Method and importance to the geochemistry of ocean island and mid-ocean ridge basalts. *Earth and Planetary Science Letters*, *230*(1-2), 29–46.

Jennings, E. S., & Holland, T. J. B. (2015). A simple thermodynamic model for melting of peridotite in the system NCFMASOCr. *Journal of Petrology*, *56*(5), 869–892. doi: 10.1093/petrology/egv020

Jones, R. E., van Keken, P. E., Hauri, E. H., Tucker, J. M., Vervoort, J., & Ballentine, C. J. (2019). Origins of the terrestrial Hf-Nd mantle array: evidence from a combined geodynamical-geochemical approach. *Earth and Planetary Science Letters*, *518*, 26–39.

Jones, T., Davies, D., Campbell, I., Wilson, C., & Kramer, S. (2016). Do mantle plumes preserve the heterogeneous structure of their deep-mantle source? *Earth and Planetary Science Letters*, *434*, 10–17.

Jones, T. D., Sime, N., & van Keken, P. (2021). Burying Earth's primitive mantle in the slab graveyard. *Geochemistry, Geophysics, Geosystems*, *22*(3), e2020GC009396.

Jordan, T. H. (1978). Composition and development of the continental tectosphere. *Nature*, *274*(5671), 544.

Katz, R. F. (2008). Magma dynamics with the enthalpy method: Benchmark solutions and magmatic focusing at mid-ocean ridges. *Journal of Petrology*, *49*(12), 2099–2121.

Katz, R. F., Spiegelmann, M., & Langmuir, C. H. (2003). A new parameterization of hydrous mantle melting. *Geochemistry, Geophysics, Geosystems*, *4*(9). doi: 10.1029/2002GC000433

Katz, R. F., & Weatherley, S. M. (2012). Consequences of mantle heterogeneity for melt extraction at mid-ocean ridges. *Earth and Planetary Science Letters*, *335*, 226–237.

Kay, R. W., & Gast, P. W. (1973). The rare earth content and origin of alkali-rich basalts. *The Journal of Geology*, *81*(6), 653–682.

Keller, T., Katz, R. F., & Hirschmann, M. M. (2017). Volatiles beneath mid-ocean ridges: Deep melting, channelised transport, focusing, and metasomatism. *Earth and Planetary Science Letters*, *464*, 55–68.

Kennett, B. L. N., & Davies, D. R. (2020). Intra-plate volcanism in North Queensland and eastern new Guinea: A cryptic mantle plume? *Gondwana Research*, *79*, 209–216.

Kimura, J.-I., & Kawabata, H. (2014). Trace element mass balance in hydrous adiabatic mantle melting: The Hydrous Adiabatic Mantle Melting Simulator version 1 (HAMMS1). *Geochemistry, Geophysics, Geosystems*, *15*(6), 2467–2493.

King, S. D., & Anderson, D. L. (1998). Edge-driven convection. *Earth and Planetary Science Letters*, *160*(3-4), 289–296.

Klein, E. M., & Langmuir, C. H. (1987). Global correlations of ocean ridge basalt chemistry with axial depth and crustal thickness. *Journal of Geophysical Research: Solid Earth*, *92*(B8), 8089–8115.

Korenaga, J., & Karato, S.-I. (2008). A new analysis of experimental data on olivine rheology. *Journal of Geophysical Research: Solid Earth*, *113*(B2).

Kramer, S. C., Davies, D. R., & Wilson, C. R. (2021). Analytical solutions for mantle flow in cylindrical and spherical shells. *Geoscientific Model Development*, *14*(4), 1899–1919.

Kramer, S. C., Wilson, C. R., & Davies, D. R. (2012). An implicit free-surface algorithm for geodynamical simulations. *Phys. Earth Planet. Int.*, *194*, 25–37. doi: 10.1016/j.pepi.2012.01.001

Krein, S. B., Behn, M. D., & Grove, T. L. (2020). Origins of Major Element, Trace Element, and Isotope Garnet Signatures in Mid-Ocean Ridge Basalts. *Journal of Geophysical Research: Solid Earth*, *125*(12), e2020JB019612.

Lachenbruch, A. H. (1970). Crustal temperature and heat production: Implications of the linear heat-flow relation. *Journal of Geophysical Research*, *75*(17), 3291–3300.

Lambart, S., Baker, M. B., & Stolper, E. M. (2016). The role of pyroxenite in basalt genesis: Melt-PX, a melting parameterization for mantle pyroxenites between 0.9 and 5 GPa. *Journal of Geophysical Research: Solid Earth*, *121*(8), 5708–5735.

Lambart, S., Laporte, D., Provost, A., & Schiano, P. (2012). Fate of pyroxenite-derived melts in the peridotitic mantle: thermodynamic and experimental constraints. *Journal of Petrology*, *53*(3), 451–476.

Landwehr, D., Blundy, J., Chamorro-Perez, E. M., Hill, E., & Wood, B. (2001). U-series disequilibria generated by partial melting of spinel lherzolite. *Earth and Planetary Science Letters*, *188*(3-4), 329–348.

Langmuir, C. H., Bender, J., Bence, A., Hanson, G., & Taylor, S. (1977). Petrogenesis of basalts from the FAMOUS area: Mid-Atlantic Ridge. *Earth and Planetary Science Letters*, *36*(1), 133–156.

Langmuir, C. H., Klein, E. M., & Plank, T. (1992). Petrological systematics of mid-ocean ridge basalts: Constraints on melt generation beneath ocean ridges. *Mantle Flow and Melt Generation at Mid-Ocean Ridges*, *71*, 183–280.

Lees, M. E., Rudge, J. F., & McKenzie, D. (2020). Gravity, Topography, and Melt Generation Rates From Simple 3-D Models of Mantle Convection. *Geochemistry, Geophysics, Geosystems*, *21*(4), e2019GC008809.

Maclennan, J., McKenzie, D., & Gronvold, K. (2001). Plume-driven upwelling under Central Iceland. *Earth and Planetary Science Letters*, *194*(1-2), 67–82.

Mallmann, G., & O'Neill, H. S. C. (2007). The effect of oxygen fugacity on the partitioning of Re between crystals and silicate melt during mantle melting. *Geochimica et Cosmochimica Acta*, *71*(11), 2837–2857.

Mathews, C. (2021). *Methods for tracking material properties within an unstructured, adaptive mesh computational modelling framework, with application to simulating the development of seismic anisotropy at spreading centres and transform faults* (Unpublished doctoral dissertation). Australian National University.

McDonough, W. F., & Sun, S. S. (1995). The composition of the Earth. *Chemical Geology*, *120*(3-4), 223–253. doi: 10.1016/0009-2541(94)00140-4

McKenzie, D. (1984). The generation and compaction of partially molten rock. *Journal of petrology*, *25*(3), 713–765.

McKenzie, D., & Bickle, M. J. (1988). The volume and composition of melt generated by extension of the lithosphere. *Journal of Petrology*, *29*(3), 625–679.

McKenzie, D., & O'Nions, R. K. (1991). Partial melt distributions from inversion of rare-earth element concentrations. *Journal of Petrology*, *32*(5), 1021–1091.

McKenzie, D., & O'Nions, R. K. (1995). The Source Regions of Ocean Island Basalts. *Journal of Petrology*, *36*(1), 133–159.

Michael, P. (1995). Regionally distinctive sources of depleted MORB: Evidence from trace elements and H_2O. *Earth and Planetary Science Letters*, *131*(3–4), 301–320. doi: 10.1016/0012-821X(95)00023-6

Morgan, W. J. (1968). Rises, trenches, great faults, and crustal blocks. *Journal of Geophysical Research*, *73*(6), 1959–1982.

Nakagawa, T., Tackley, P. J., Deschamps, F., & Connolly, J. A. (2010). The influence of morb and harzburgite composition on thermo-chemical mantle convection in a 3-d spherical shell with self-consistently calculated mineral physics. *Earth and Planetary Science Letters*, *296*(3-4), 403–412.

Niu, Y. (2016). The meaning of global ocean ridge basalt major element compositions. *Journal of Petrology*, *57*(11-12), 2081–2103.

Niu, Y., & O'Hara, M. J. (2008). Global correlations of ocean ridge basalt chemistry with axial depth: a new perspective. *Journal of Petrology*, *49*(4), 633–664.

Niu, Y., Wilson, M., Humphreys, E. R., & O'Hara, M. J. (2011). The origin of intra-plate ocean island basalts (OIB): The lid effect and its geodynamic implications. *Journal of Petrology*, *52*(7-8), 1443–1468.

O'Hara, M. (1977). Geochemical evolution during fractional crystallisation of a periodically refilled magma chamber. *Nature*, *266*(5602), 503–507.

O'Hara, M. (1985). Importance of the "shape" of the melting regime during partial melting of the mantle. *Nature*, *314*(6006), 58–62.

O'Neill, H. S. C., & Jenner, F. E. (2012). The global pattern of trace-element distributions in ocean floor basalts. *Nature*, *491*(7426), 698–704.

O'Neill, H. S. C., & Jenner, F. E. (2016). Causes of the compositional variability among ocean floor basalts. *Journal of Petrology*, *57*(11-12), 2163–2194.

Perrin, A., Goes, S., Prytulak, J., Rondenay, S., & Davies, D. R. (2018). Mantle wedge temperatures and their potential relation to volcanic arc location. *Earth and Planetary Science Letters*, *501*, 67–77.

Petzold, L. (1983). Automatic selection of methods for solving stiff and nonstiff systems of ordinary differential equations. *SIAM journal on scientific and statistical computing*, *4*(1), 136–148.

Plank, T., & Langmuir, C. H. (1992). Effects of the melting regime on the composition of the oceanic crust. *Journal of Geophysical Research: Solid Earth*, *97*(B13), 19749–19770.

Pollack, H. N., & Chapman, D. S. (1977). Mantle heat flow. *Earth and Planetary Science Letters*, *34*(2), 174–184.

Rawlinson, N., Davies, D. R., & Pilia, S. (2017). The mechanisms underpinning Cenozoic intraplate volcanism in eastern Australia: Insights from seismic tomography and geodynamic modeling. *Geophysical Research Letters*, *44*(19), 9681–9690.

Rees Jones, D. W., Katz, R. F., Tian, M., & Rudge, J. F. (2018). Thermal impact of magmatism in subduction zones. *Earth and Planetary Science Letters*, *481*, 73–79.

Richards, F. D., Hoggard, M. J., White, N., & Ghelichkhan, S. (2020). Quantifying the relationship between short-wavelength dynamic topography and thermomechanical structure of the upper mantle using calibrated parameterization of anelasticity. *Journal of Geophysical Research: Solid Earth*, e2019JB019062.

Salters, V. J. M., & Stracke, A. (2004). Composition of the depleted mantle. *Geochemistry, Geophysics, Geosystems*, *5*(5). doi: 10.1029/2003GC000597

Schaeffer, A. J., & Lebedev, S. (2013). Global shear speed structure of the upper mantle and transition zone. *Geophysical Journal International*, *194*(1), 417–449. doi: 10.1093/gji/ggt095

Schatz, J. F., & Simmons, G. (1972). Thermal conductivity of earth materials at high temperatures. *Journal of Geophysical Research*, *77*(35), 6966–6983.

Schellart, W. P., Freeman, J., Stegman, D. R., Moresi, L., & May, D. (2007). Evolution and diversity of subduction zones controlled by slab width. *Nature*, *446*(7133), 308–311.

Shannon, R. D. (1976). Revised effective ionic radii and systematic studies of interatomic distances in halides and chalcogenides. *Acta crystallographica section A: crystal physics, diffraction, theoretical and general crystallography*, *32*(5), 751–767.

Shaw, D. M. (1970). Trace element fractionation during anatexis. *Geochimica et Cosmochimica Acta*, *34*, 237–243.

Shaw, D. M. (1979). Trace element melting models. *Physics and Chemistry of the Earth*, *11*, 577–586.

Shorttle, O., Maclennan, J., & Lambart, S. (2014). Quantifying lithological variability in the mantle. *Earth and Planetary Science Letters*, *395*, 24–40.

Sim, S. J., Spiegelman, M., Stegman, D. R., & Wilson, C. (2020). The influence of spreading rate and permeability on melt focusing beneath mid-ocean ridges. *Physics of the Earth and Planetary Interiors*, *304*, 106486.

Steinberger, B. (2000). Plumes in a convecting mantle: Models and observations for individual hotspots. *Journal of Geophysical Research: Solid Earth*, *105*(B5), 11127–11152.

Stracke, A. (2012). Earth's heterogeneous mantle: a product of convection-driven interaction between crust and mantle. *Chemical Geology*, *330*, 274–299.

Stracke, A., Bourdon, B., & McKenzie, D. (2006). Melt extraction in the Earth's mantle: constraints from U–Th–Pa–Ra studies in oceanic basalts. *Earth and Planetary Science Letters*, *244*(1-2), 97–112.

Sun, C., & Liang, Y. (2012). Distribution of REE between clinopyroxene and basaltic melt along a mantle adiabat: effects of major element composition, water, and temperature. *Contributions to Mineralogy and Petrology*, *163*(5), 807–823.

Sun, C., & Liang, Y. (2013). The importance of crystal chemistry on REE partitioning between mantle minerals (garnet, clinopyroxene, orthopyroxene, and olivine) and basaltic melts. *Chemical Geology*, *358*, 23–36.

Tackley, P. J., Stevenson, D. J., Glatzmaier, G. A., & Schubert, G. (1993). Effects of an endothermic phase transition at 670 km depth in a spherical model of convection in the Earth's mantle. *Nature*, *361*(6414), 699–704.

Till, C. B., Grove, T. L., & Krawczynski, M. J. (2012). A melting model for variably depleted and enriched lherzolite in the plagioclase and spinel stability fields. *Journal of Geophysical Research: Solid Earth*, *117*(B6).

Turcotte, D. L., & Emerman, S. H. (1983). Mechanisms of active and passive rifting. In *Developments in geotectonics* (Vol. 19, pp. 39–50). Elsevier.

van Heck, H. J., Davies, J. H., Elliott, T., & Porcelli, D. (2016). Global-scale modelling of melting and isotopic evolution of Earth's mantle: melting modules for TERRA. *Geoscientific Model Development*, *9*(4), 1399–1411.

Walter, M. J. (1998). Melting of garnet peridotite and the origin of komatiite and depleted lithosphere. *Journal of Petrology*, *39*(1), 29–60. doi: 10.1093/petrology/39.1.29

Watson, S., & M^{c}Kenzie, D. (1991). Melt generation by plumes: a study of Hawaiian volcanism. *Journal of Petrology*, *32*(3), 501–537.

Wessel, P., Smith, W. H., Scharroo, R., Luis, J., & Wobbe, F. (2013). Generic mapping tools: improved version released. *Eos, Transactions American Geophysical Union*, *94*(45), 409–410.

White, R. S., M^{c}Kenzie, D., & O'Nions, R. K. (1992). Oceanic Crustal Thickness From Seismic Measurements and Rare Earth Element Inversions. *Journal of Geophysical Research*, *97*, 19683-19715.

White, R. S., Minshull, T. A., Bickle, M. J., & Robinson, C. J. (2001). Melt generation at very slow-spreading oceanic ridges: Constraints from geochemical and geophysical data. *Journal of Petrology*, *42*(6), 1171–1196.

Wood, B. J., & Banno, S. (1973). Garnet-orthopyroxene and orthopyroxene-clinopyroxene relationships in simple and complex systems. *Contributions to Mineralogy and Petrology*, *42*(2), 109–124.

Wood, B. J., & Blundy, J. D. (1997). A predictive model for rare earth element partitioning between clinopyroxene and anhydrous silicate melt. *Contributions to Mineralogy and Petrology*, *129*(2-3), 166–181.

Wood, B. J., & Blundy, J. D. (2014). Trace element partitioning: the influences of ionic radius, cation charge, pressure, and temperature. In H. D. Holland & K. K. Turekian (Eds.), *Treatise on geochemistry* (Vol. 3, pp. 421–448). Elsevier.

Yao, L., Sun, C., & Liang, Y. (2012). A parameterized model for REE distribution between low-Ca pyroxene and basaltic melts with applications to REE partitioning in low-Ca pyroxene along a mantle adiabat and during pyroxenite-derived melt and peridotite interaction. *Contributions to Mineralogy and Petrology*, *164*(2), 261–280.

Yaxley, G. M., & Green, D. H. (1998). Reactions between eclogite and peridotite: mantle refertilisation by subduction of oceanic crust. *Schweiz. Mineral. Petrogr. Mitt*, *78*(2), 243–255.